RESEARCH ARTICLE

Coupled atmosphere–ocean observations of a cold-air outbreak and its impact on the Iceland Sea

Ian A. Renfrew[1] 🔵 | Jie Huang[2] | Stefanie Semper[2,3] 🔵 | Christopher Barrell[1] |
Annick Terpstra[1,3] | Robert S. Pickart[2] | Kjetil Våge[3] | Andrew D. Elvidge[1] |
Thomas Spengler[3] | Anna-Marie Strehl[3] | Alexandra Weiss[4]

[1]School of Environmental Sciences, University of East Anglia, Norwich, UK

[2]Woods Hole Oceanographic Institution, Woods Hole, Massachusetts USA

[3]Geophysical Institute, University of Bergen and Bjerknes Centre for Climate Research, Bergen, Norway

[4]British Antarctic Survey, Cambridge, UK

Correspondence
Ian A. Renfrew, Centre for Ocean and Atmospheric Sciences, School of Environmental Sciences, University of East Anglia, Norwich Research Park, Norwich, NR4 7TJ, UK.
Email: i.renfrew@uea.ac.uk

Abstract

Marine cold-air outbreaks (CAOs) are vigorous equatorward excursions of cold air over the ocean, responsible for the majority of wintertime oceanic heat loss from the subpolar seas of the North Atlantic. However, the impact of individual CAO events on the ocean is poorly understood. Here we present the first coupled observations of the atmosphere and ocean during a wintertime CAO event, between 28 February and 13 March 2018, in the subpolar North Atlantic region. Comprehensive observations are presented from five aircraft flights, a research vessel, a meteorological buoy, a subsurface mooring, an ocean glider, and an Argo float. The CAO event starts abruptly with substantial changes in temperature, humidity and wind throughout the atmospheric boundary layer. The CAO is well mixed vertically and, away from the sea-ice edge, relatively homogeneous spatially. During the CAO peak, higher sensible heat fluxes occupy at least the lowest 200 m of the atmospheric boundary layer, while higher latent heat fluxes are confined to the surface layer. The response of the ocean to the CAO is spatially dependent. In the interior of the Iceland Sea the mixed layer cools, while in the boundary current region it warms. In both locations, the mixed layer deepens and becomes more saline. Combining our observations with one-dimensional mixed-layer modelling, we show that in the interior of the Iceland Sea, atmospheric forcing dominates the ocean response. In contrast, in the boundary current region lateral advection and mixing counteract the short-term impact of the atmospheric forcing. Time series observations of the late-winter period illustrate a highly variable ocean mixed layer, with lateral advection and mixing often masking the ocean's general cooling and deepening response to individual CAO events.

KEYWORDS

cold-air outbreak, *in situ* observations, mixed-layer depth, Nordic Seas, subpolar seas, turbulent fluxes

1 | INTRODUCTION

Marine cold-air outbreaks (CAOs) are excursions of cold, dry polar air streaming off sea ice, or cold landmasses, over relatively warm ocean water. They lead to strong upward surface turbulent heat and moisture fluxes (Papritz and Spengler, 2017; Terpstra *et al.*, 2021). The fluxes warm the atmospheric surface layer, reducing the stratification and triggering shallow atmospheric convection, that can often be visualised via convective cloud streets or cells (e.g., Atkinson and Wu Zhang, 1996). The accumulated surface turbulent sensible and latent heat fluxes associated with marine CAOs also cool and salinize the surface ocean. In key regions, such as the subpolar seas of the North Atlantic, this ocean densification is a critical component of the global ocean circulation: it drives the convective over-turning that contributes dense waters to the lower limb of the Atlantic Meridional Overturning Circulation (AMOC; Buckley and Marshall, 2016). Arguably, the subpolar seas of the North Atlantic are where 'communication' between the atmosphere and ocean is most critical, and CAOs are the dominant medium for that communication in winter (Buckley and Marshall, 2016; Papritz and Spengler, 2017; Renfrew *et al.*, 2019). However, the impact of individual CAO events on the ocean is poorly known.

CAOs are generally synoptic in scale (>1,000 km) and duration, for example, median durations of 2.5–3 days and durations of a week on occasion (Harden *et al.*, 2015; Terpstra *et al.*, 2021). They are driven by a variety of meteoro-logical conditions. The strongest CAOs tend to occur to the rear (i.e., in the western portion) of synoptic-scale cyclones that track towards higher latitudes (Kolstad *et al.*, 2009; Fletcher *et al.*, 2016; Terpstra *et al.*, 2021). However, they are also commonly associated with longitudinal pressure gradients between cyclones and anticyclones (Fletcher *et al.*, 2016; Papritz and Grams, 2018), or with orographic flows such as barrier winds, tip jets, and katabatic flows (Outten *et al.*, 2009; Renfrew *et al.*, 2009; Våge *et al.*, 2009; Harden *et al.*, 2011; Oltmanns *et al.*, 2014).

The observed thermodynamic and turbulent char-acteristics of marine CAOs have been documented in various studies, most commonly using aircraft obser-vations. Notable North Atlantic case studies include a well-studied extreme CAO over the Gulf Stream (Bane Jr and Osgood, 1989; Grossman and Betts, 1990; Chou and Ferguson, 1991); an extreme CAO over the Labrador Sea (Renfrew and Moore, 1999; Pagowski and Moore, 2001); a collection of case studies over the Greenland and Norwe-gian Seas (Brümmer, 1996, 1997, 1999); and a collection of cases over the Mediterranean Sea (Brilouet *et al.*, 2017). Common features include: an atmospheric boundary layer (ABL) that warms, moistens, and deepens with down-stream distance encompassing an unstable surface layer and a capping inversion; higher turbulent momentum and heat fluxes that decrease rapidly with height through the ABL; and the development of clouds with down-stream distance. Coherent ABL circulations are common and, given sufficient wind speed, feature roll vortices (visualised as cloud streets), often giving way to open or closed cells downstream (Atkinson and Wu Zhang, 1996; Brümmer, 1999; Pithan *et al.*, 2018). These coherent structures contribute to the surface turbulent heat fluxes (Brümmer, 1999; Spensberger and Spengler, 2021; Duscha *et al.*, 2022), which are the largest sources of heat and mois-ture to the ABL as the CAO warms and moistens with fetch (Brümmer, 1997).

Numerical models can capture the salient thermo-dynamic and turbulent features of CAOs given suf-ficient resolution and suitable parameterizations (e.g., Pagowski and Moore, 2001; Liu *et al.*, 2004). However, there are sensitivities in their response to the marginal ice zone (Liu *et al.*, 2006; Gryschka *et al.*, 2008; Chechin *et al.*, 2013; Spensberger and Spengler, 2021) and chal-lenges in the forecasting of embedded mesoscale weather systems such as polar lows (e.g., Sergeev *et al.*, 2017, 2018). Around two thirds of CAO events are associated with polar meso-cyclogenesis (Terpstra *et al.*, 2021; see also Michel et al. 2018). Furthermore, simulating the distribu-tion and phase of the clouds that develop within CAOs remains a major challenge (e.g., Geerts *et al.*, 2022), both for convection-permitting operational models (e.g., Abel *et al.*, 2017) and large eddy simulations (e.g., De Roode *et al.*, 2019).

CAOs occur over the subpolar seas of all the major oceans. They tend to be stronger in the Northern Hemi-sphere, due to the positioning of cold air masses residing over land or pack ice near relatively warm water, with notable peaks over the Kuroshio, Bering Sea, Gulf Stream, Labrador Sea, Barents Sea, and the Nordic Seas (the Norwegian, Greenland, and Iceland Seas) – see Fletcher *et al.* (2016). All of these regions are prone to extremes in the distribution of surface heat fluxes (Gulev and Belyaev, 2012).

CAOs are key to the climate system via both the atmosphere and ocean. They are one component of the exchange of energy in the atmosphere between the polar regions and mid-latitudes (Iwasaki *et al.*, 2014; Pithan *et al.*, 2018), and they are responsible for 60%–80% of the wintertime oceanic heat loss in critical oceanic regions such as the subpolar seas of the North Atlantic (Papritz and Spengler, 2017). Papritz and Spengler (2017) show that this heat loss is mainly connected to intense CAOs in the north-ern Greenland Sea and eastern Barents Sea, combined with more frequent weak-to-moderate CAOs in the Nor-wegian, Irminger, and Iceland Seas. Following a median air parcel through a CAO, the surface turbulent heat fluxes

increase rapidly, from approximately 0 to approximately $300 \, \mathrm{W \cdot m^{-2}}$, before decreasing more slowly over a few days in an evolution that is common for all subregions of the North Atlantic (Papritz and Spengler, 2017). The sensible heat fluxes dominate the latent fluxes for cold-water locations, such as the Greenland, Barents, and Iceland Seas, while the opposite is true for the warmer waters of the Norwegian and Irminger Seas. These characteristics are consistent with an analysis of CAO events by Terpstra *et al.* (2021).

Previous studies have examined the impact of surface heat fluxes on the ocean mixed layer in the subpolar seas; for example, over the Irminger Sea (Våge *et al.*, 2008), Iceland Sea (Moore *et al.*, 2015; Våge *et al.*, 2015; Våge *et al.*, 2018), Greenland Sea (Schott *et al.*, 1993; Moore *et al.*, 2015; Brakstad *et al.*, 2019), Norwegian Sea (Sætra *et al.*, 2008; Isachsen *et al.*, 2013), Labrador Sea (Lilly *et al.*, 1999; Steffen and D'Asaro, 2002), and Barents Sea (Skagseth *et al.*, 2020). However, these studies have focused on integrated changes in the ocean mixed layer over the extended winter season and have relied on meteorological reanalyses (or similar) for atmospheric forcing data. They have not examined the detailed ocean response to an individual CAO event, nor have they had available *in-situ* observations from the atmosphere.

The Iceland Sea has been a particular focus of attention in the last decade. The recently identified North Icelandic Jet that transports dense water along the slope north of Iceland into Denmark Strait revitalized interest in water mass transformation in this region (Jónsson and Valdimarsson, 2004; Våge *et al.*, 2011; Semper *et al.*, 2019). This rekindled an earlier hypothesis that the central Iceland Sea is a location of significant dense water formation (Swift *et al.*, 1980; Swift and Aagaard, 1981). In the present climate, the bulk of dense water transported by the North Icelandic Jet originates in the Greenland Sea (Huang *et al.*, 2020), as the waters formed in the Iceland Sea have become less dense (Våge *et al.*, 2015; Semper *et al.*, 2022). However, only a few decades ago, when sea ice extended farther off the Greenland shelf, the central Iceland Sea was likely a more significant source of dense water (Våge *et al.*, 2022). A dramatic reduction in sea ice has made much of the western part of the Iceland Sea directly accessible to the atmosphere in winter, thereby exposing new regions where water mass transformation takes place (Våge *et al.*, 2018; Moore *et al.*, 2022) and shifting the locus of dense water formation from the central to the western Iceland Sea (Våge *et al.*, 2022).

The CAO analysed here occurred in the western Iceland Sea. We use data collected during the Iceland–Greenland Seas Project (IGP), an extensive atmosphere–ocean field campaign that took place in winter 2018; see Renfrew *et al.* (2019) for an overview of the

IGP and further background. One goal of the IGP was to determine the location and causes of dense water formation by CAOs. The observational program was the first time that simultaneous *in-situ* observations of the atmosphere and ocean were obtained in the subpolar seas of the North Atlantic. As such, our case study is, to our knowledge, the first subpolar CAO event to be analysed from a coupled atmosphere–ocean perspective. (We note that Duscha *et al.*, 2022 examines coherent structures within the ABL of this CAO event, primarily via ship-based Doppler Lidar wind measurements). We focus on the immediate ocean response to this multi-day CAO event in late winter. For the atmosphere, we use observations from five aircraft flights and continuous measurements from a research vessel and a buoy. For the ocean, we use data from roughly 200 hydrographic casts from the research vessel, a glider, and an Argo float, and continuous measurements from a mooring. Our objectives are:

- to quantify the event via CAO metrics
- to document the thermodynamic and turbulent ABL structure
- to document the response of the ocean's mixed layer over space and time
- to investigate the mechanisms that dictate this ocean response.

The ocean response is also placed into a seasonal context using *in-situ* time series observations.

2 | DATA SETS AND METHODOLOGY

An overview of the research platforms, observing systems, research cruise, flight campaign, and sustained observations can be found in Renfrew *et al.* (2019). Here we provide a brief description of the pertinent datasets and outline our observational coordination strategy.

2.1 | Atmospheric observations

Near-surface observations from a Seawatch Wavescan meteorological buoy located in the northwest Iceland Sea at $70^{\circ}38.38$ N, $15^{\circ}24.58$ W were made between 17 February and 5 May 2018 (see Figure 1 for location). Hourly observations of air temperature, relative humidity (RH), air pressure, solar radiation, wind speed, and wind direction were made at a height of approximately 3 m. Further details and quality control are described in Renfrew *et al.* (2021).
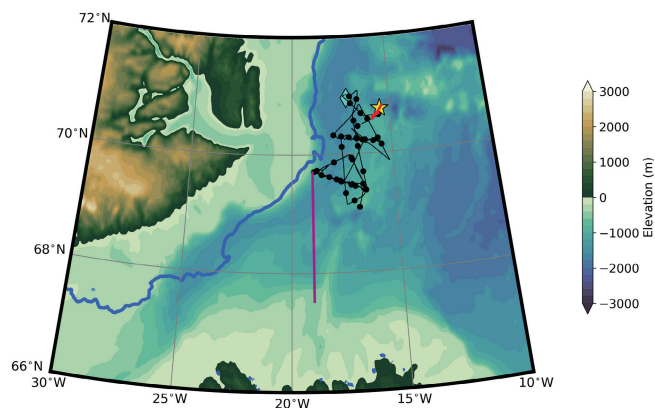
FIGURE 1 Map of the study area, where the topography and bathymetry are shaded. Overlain for the period 28 February to 8 March 2018 are the 0.2 sea-ice fraction contour from Advanced Microwave Scanning Radiometer 2 (AMSR2) data (blue line), the track of the research vessel (black line), the location of radiosonde releases (black dots), the location of the Eggvin offset mooring and the meteorological buoy (yellow star), the mean location of the glider (cyan diamond), the track of the Argo float (red line), and the location of the aircraft cross-section on 1 March 2018 (purple line; cf. Figure 6) [Colour figure can be viewed at wileyonlinelibrary.com]

Surface-layer observations were conducted from the research vessel *Alliance* throughout a 43-day cruise in February and March 2018. Air temperature, pressure, and RH (WeatherPak) were taken at approximately 15 m above sea level on the bow mast and combined with wind speed and wind direction from the lowest bin (40 m) of a Doppler wind Lidar (a Leosphere WindCube v2 8.66, Helsinki, Finland) located on the boat deck. A novel correction algorithm for translational motions of the ship, as well as established corrections for the pitch, roll, and yaw of the *Alliance*, based on inertial motion unit measurements were implemented (see Duscha *et al.*, 2022). Sea surface temperature (SST) was measured by the thermosalinograph (intake depth of 2.5 m). Further details and quality control are described in Renfrew *et al.* (2021). We released 100 Vaisala RS41-SG (Helsinki, Finland) radiosondes during the cruise, including 39 during the CAO event (see Figure 1). Radiosonde profiles from the mountainous island of Jan Mayen (WMO station 01001) were also examined. Surface turbulent flux estimates using the buoy and research vessel observations were made using the COARE3 bulk flux algorithm (Fairall *et al.*, 2003).

Low-level observations from a research aircraft, a DH6 Twin Otter, are also utilised. Five flights were made during the CAO event, four of them coordinated with the research vessel. We examine surface layer and ABL observations, made on straight and level legs or as 'sawtooth' ABL profiles. The legs were divided into 'flux runs' of 150 s (~9 km) to estimate turbulent fluxes using the

covariance method (see Petersen and Renfrew, 2009 and Elvidge *et al.*, 2016 for details). Extensive quality control procedures were implemented, as described in Renfrew *et al.* (2021) and Elvidge *et al.* (2021).

2.2 | Oceanographic observations

Shipboard hydrographic data in the western Iceland and Greenland Seas were collected on the *Alliance* whose cruise track during the CAO event is shown in Figure 1. Vertical profiles of temperature and salinity were obtained using two types of instruments: (i) a conductivity–temperature-depth (CTD) system, attached to a rosette with twelve 5-L Niskin bottles for seawater sampling; and (ii) expendable CTDs (XCTDs) and bathythermographs (XBTs), which were used in inclement weather or to save time. The CTD conductivity sensors were calibrated using the water sample salinity data. The resulting accuracies of the CTD measurements are 0.3 dbar for pressure, 0.001°C for temperature, and 0.009 for salinity. Here we use potential temperature referenced to the sea surface (temperature), practical salinity (salinity), and potential density referenced to the sea surface. The XCTD and XBT profiles were calibrated by comparing a set of simultaneous XCTD/XBT and CTD profiles. Overall, the accuracy of the expendable measurements is estimated to be about the same as that of the CTD. Further details on shipboard data processing and calibration are described in Huang *et al.* (2021). During the CAO event, a total of 137 temperature profiles (36 CTDs, 62 XCTDs, and 39 XBTs) and 98 salinity profiles (36 CTDs and 62 XCTDs) were made from the research vessel. The vertical resolution of the final quality-controlled profiles is 2 dbar for the CTD and 2 m for the expendables.

Additional hydrographic profiles were provided by an Argo float (ID: Coriolis 3,901,988), deployed from the *Alliance* on February 28, 2018. The float drifted at 200 m depth during the CAO event and recorded daily CTD profiles between 1,000 m and the surface within the Eggvin Offset – a deep passage between the West Jan Mayen Ridge and the Kolbeinsey Ridge (see Figure 1 for the drift track). The shallow parking depth ensured that the float spent most of the time freely drifting within the mixed layer. We use the standard delayed-mode Argo data, which have a nominal accuracy of ±0.002°C for temperature, ±0.01 for salinity, and 2 dbar for pressure (Wong *et al.*, 2020). A comparison to concurrent shipboard CTD data prompted a bias correction in salinity of −0.0095.

A SeaGlider deployed from the *Alliance* collected data along a section near 71° N from the East Greenland continental slope to the Eggvin Offset. The glider sampled temperature, salinity, and pressure at 8–30 s intervals

which corresponds to a vertical resolution of 0.5–3 dbar. The glider data have a nominal accuracy of $\pm 0.001°$C for temperature and ± 0.01 for salinity. The sensors were laboratory-calibrated prior to deployment and against shipboard measurements by comparing the mean profiles below 500 m depth, prompting a bias correction in salinity of -0.006. Following Våge et al. (2018), each dive and climb profile was subsequently inspected for density inversions, and measurements associated with inversions exceeding $0.03 \text{ kg} \cdot \text{m}^{-3}$ were excluded.

Hydrographic time series were obtained from a subsurface mooring deployed on the southern flank of the Eggvin Offset at 70°37.75 N, 15°36.41 W from 27 August 2016 to 7 June 2018 (see Figure 1). The mooring was equipped with five point-CTD sensors and 16 temperature loggers. The vertical resolution of the temperature sensors was exceptionally high: 25 m in the upper 200 m of the water column and 50 m down to 800 m depth. The shallowest measurement depth was 8 m. The five CTDs consisted of four MicroCATS located at 8 m, 111 m, 675 m, and 1,186 m, and one Aanderaa SeaGuard at 386 m. The hydrographic sensors were calibrated by comparison with three shipboard CTD casts at the mooring location during the deployment period. None of the temperature sensors above a depth of 500 m required corrections for drift or offset. The initial mooring accuracies for all Sea-Bird Electronics instruments (the Aanderaa SeaGuard) are $\pm 0.002°$C ($\pm 0.03°$C) for temperature and 0.003–0.004 (± 0.019–0.026) for salinity considering our temperature range of -1–8°C. The temporal resolution of the measurements ranged from 30 s (five SBE56 temperature loggers) to 15 min (four SBE37 MicroCATs and 11 SBE39 temperature loggers) and 30 min (one Aanderaa SeaGuard). Data from the high-frequency temperature loggers were first averaged into 15-min intervals, then all data were interpolated onto a common 15-min time base. This resulted in a total of 864 moored temperature profiles during the CAO event.

2.3 | Reanalyses and satellite products

We use output from ERA5, the fifth generation ECMWF atmospheric reanalysis which is produced using cycle 41r2 of the Integrated Forecast System model, using a four-dimensional variational data assimilation scheme (Hersbach et al., 2020). The reanalysis benefits from a relatively high-resolution grid with 137 vertical levels and a horizontal grid spacing of 0.28125° (~31 km, from a T639 triangular truncation). We use instantaneous meteorological variables and hourly-mean surface fluxes output every 3 hr. An evaluation of ERA5 surface-layer meteorology and surface turbulent fluxes for the Iceland and Greenland Seas showed that it generally compares very well to observations, although it is less accurate over the marginal ice zone than over open water (Renfrew et al., 2021). For 2007 onwards, ERA5 uses the UK Met Office's Operational Sea-surface Temperature and Sea Ice Analysis (OSTIA) for daily SST and sea-ice fields. Renfrew et al. (2021) demonstrate that the OSTIA sea-ice distribution is overly smooth compared to aircraft- and satellite-based observations, so here we also use sea-ice fraction derived from the Advanced Microwave Scanning Radiometer 2 (AMSR2), following Spreen et al. (2008).

2.4 | Coordination strategy

From the outset we designed the IGP winter field campaign to take a coupled atmosphere–ocean approach for the observations. This included moving to a coordinated 'survey phase' when a CAO event was forecast (cf. Renfrew et al., 2019). In addition to global and regional weather forecasts, we had specialized CAO forecast products diagnosed from the ECMWF ensemble prediction system that allowed planning up to a week in advance. We coordinated activities on the research vessel and the aircraft via daily updates of our plans – all informed by common forecast products. This coordination allowed simultaneous and enhanced sampling of both the atmosphere (e.g., additional radiosonde releases; low-level flight legs around the ship) and ocean (e.g., rapid XBT surveys; survey triangles of CTDs or XCTDs), thus facilitating a coupled analysis.

3 | ATMOSPHERIC OBSERVATIONS OF A COLD-AIR OUTBREAK

3.1 | Synoptic overview

The CAO event began on 28 February 2018 and was remarkably long-lived, lasting 10–13 days depending on the metric used. Note we use a CAO index metric of θ_{SST} - θ_{800}, where the subscript indicates the potential temperature levels of the sea surface and at 800 hPa (e.g., Kolstad et al., 2009; Papritz and Spengler, 2017) and a CAO depth metric defined as the height in hPa where $\theta = \theta_{SST}$, which is a measure of the depth of the cold-air mass in pressure units. The CAO depth metric reflects the potential temperature and static stability of the air mass so is an integrated measure of CAO strength (see Terpstra et al., 2021). At onset, illustrated at 1200 UTC on 1 March 2018, there is widespread northerly flow and NNE-oriented isobars over the Iceland and Greenland Seas, associated with a mesoscale low that had traversed

west to east across the Iceland Sea now weakening over the Norwegian Sea (Figure 2). At its onset the CAO is weak: the CAO depth is only 100–150 hPa over the Iceland Sea, increasing to 300–350 hPa in Fram Strait. The associated surface turbulent heat fluxes are only 150–250 W·m^{-2} in the northwest Iceland Sea. At its onset, the CAO depth and surface sensible heat flux (SHF) are comparable to their ERA5 winter means and the CAO index at 800 hPa is negative – indicating no CAO by this metric – as the cold air is shallow and does not reach this level (Figure 3). The surface latent heat flux (LHF) is somewhat higher than the winter mean. At the meteorological buoy, surface-layer observations show the CAO starts with a drop in air temperature from 2 to −2.5°C, coincident with a dramatic change in wind direction and an increase in wind speed from 3 to 13 m·s^{-1}, as well as an increase in total turbulent heat fluxes (THFs) from approximately 0 to 150 W·m^{-2} (Figure 4). The surface-layer research vessel observations are very similar (not shown). In short, the CAO starts abruptly but was comparatively weak at this time over the Iceland Sea.

Over the next few days, the CAO becomes moderate in strength: the CAO index, CAO depth, and surface heat fluxes all increase to greater than +1 standard deviation (σ) above the winter mean (Figure 3). The CAO peak is on 4 March, after which the CAO index hovers around the +1σ level and the CAO depth, SHF, and LHF wax and wane, before the event tails off around 13 March. Viewed via the buoy observations, the CAO peak is marked by a minimum in air temperature of −5.5°C, a maximum in wind speed of 14 m·s^{-1}, and a maximum in THF of more than 200 W·m^{-2} (Figure 4). The rest of the event has temperatures below 0°C, and winds typically 10–12 m·s^{-1}, with a second temperature minimum on 9 March due to an enhanced off-ice flow component, before the CAO tails off.

The synoptic situation at the peak of the CAO is shown in the right column of Figure 2. At this time the CAO depth is around 350 hPa and the CAO index varies between 4 and 6 K, which is in the moderate (4–8 K) CAO category of Papritz and Spengler (2017). Across the Iceland and Greenland Seas, the winds are generally from the NNE to NE, explaining the contrast in CAO depths between the Norwegian Sea (>400 hPa) and the Iceland Sea (300–350 hPa) where the extensive upstream fetch of the air mass has warmed the ABL and decreased the CAO depth. At the time of the CAO peak, the wind vectors over the Iceland Sea are more northerly, suggesting some of the air is coming off the sea ice adjacent to the Greenland coast. Indeed, the reanalysis THF peaks at 400 W·m^{-2} just off the ice edge, decreasing rapidly with fetch to 200–250 W·m^{-2} over the NW Iceland Sea–values consistent with the buoy observations (Figure 4).

3.2 | Thermodynamic and turbulent structure

A vertical cross-section of the ABL and lower troposphere over time is provided from radiosonde profiles launched from the *Alliance* (Figure 5). This should be interpreted as a time series of the evolving CAO event as the movement of the research vessel around the 'survey triangles' is small compared to the horizontal scale of the CAO. The sharp potential temperature (θ) gradient at 0600–1200 UTC on 28 February that signals the onset of the CAO extends through the lower troposphere, while the enhanced wind speed is confined to the ABL where it peaks at 18 m·s^{-1}. This CAO front is distinct from the strong southerly winds associated with the mesoscale low. As the CAO event strengthens, the ABL deepens from about 800 to 2000 m (as evident from changes in the vertical gradients in θ and RH). The peak of the event, on 4 March, is characterized by an ABL jet of cold air sampled when the ship is within the marginal ice zone. Note that some of the higher-frequency structure in the cross-section is associated with the location of the ship; for example, there are cold and dry periods when the ship is closer to the sea ice around 1800 UTC on 1 March.

The variability in the ABL depth is related to the local wind speed (e.g., enhanced on 2 and 4 March) and the surface heat fluxes (not shown). The collapse in ABL height during 5–6 March is due to a warming of the entire lower troposphere that is associated with a more easterly wind direction (see Figure 4). One could define this as the end of the CAO event, based on the CAO depth, or surface heat fluxes, but the CAO index remains at +1σ so instead we view this as a transient weakening. Subsequent strengthening and weakening of the CAO event are evident in the buoy and ERA5 data (Figures 3, 4), but are not captured by the research vessel which left the survey region on 9 March. The onset of the CAO brings a dramatic change to the ABL which becomes neutrally stratified, above an unstable surface layer and capped by a strong θ gradient (Figure 5). The wind speed is roughly constant through the ABL (above the surface layer). The RH increases with height through the ABL and peaks at more than 90% at the top of the ABL, above which it is exceptionally dry (RH < 30%). Satellite imagery confirms that the ABL is replete with comparatively small convective cells scattered across the NW Iceland Sea on 1 March, except for a cloud-free band adjacent to the sea ice (e.g., Figure 2). Based on the RH profiles, these cumulus clouds top the ABL and are relatively shallow (typically ∼500 m thick). During 2–3 March the ABL cloud cells expand, and, by 4 March, they are larger, deeper and more convective in appearance (Figure 2). Comparing the two satellite images the change in cloud characteristics nicely illustrates the
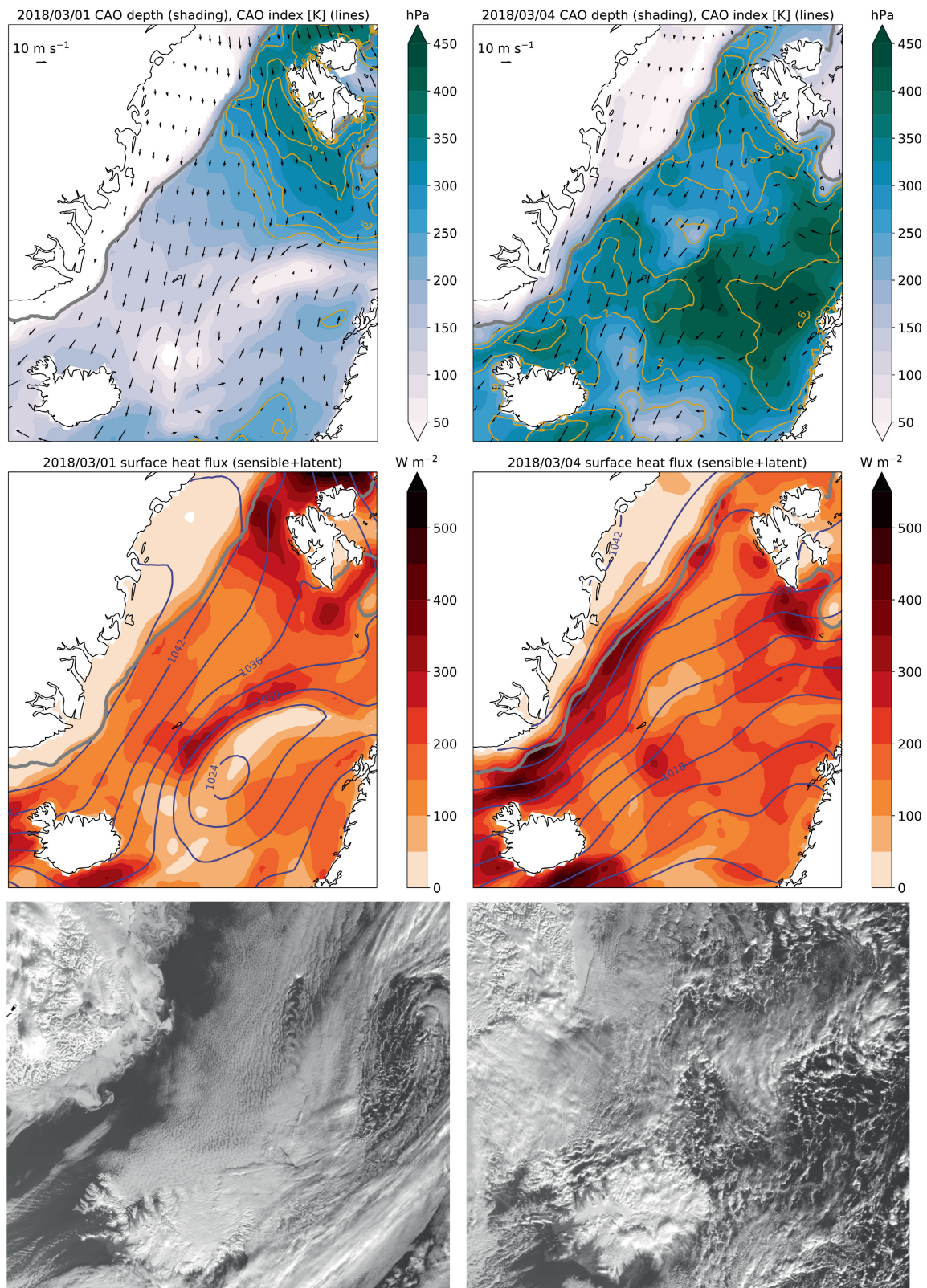
FIGURE 2 Synoptic evolution of the cold-air outbreak (CAO) showing the approximate onset at 1200 UTC 1 March (left) and the peak at 1200 UTC 4 March 2018 (right) using ERA5 output. The top panels show the CAO depth (shading, hPa), the CAO index (amber contours, K) and the wind at 800 hPa (vectors). The middle panels show the total turbulent heat flux at the surface (shading, W·m^{-2}) and m.s.l. pressure (maroon contours, hPa). A sea ice edge, taken to be the 0.2 sea-ice fraction contour, is shown on the ERA5 panels (thick grey line). The bottom panels are visible satellite images at 1143 and 1137 UTC on 1 and 4 of March from VIIRS, showing the lower-left quarter of the ERA5 domains [Colour figure can be viewed at wileyonlinelibrary.com]
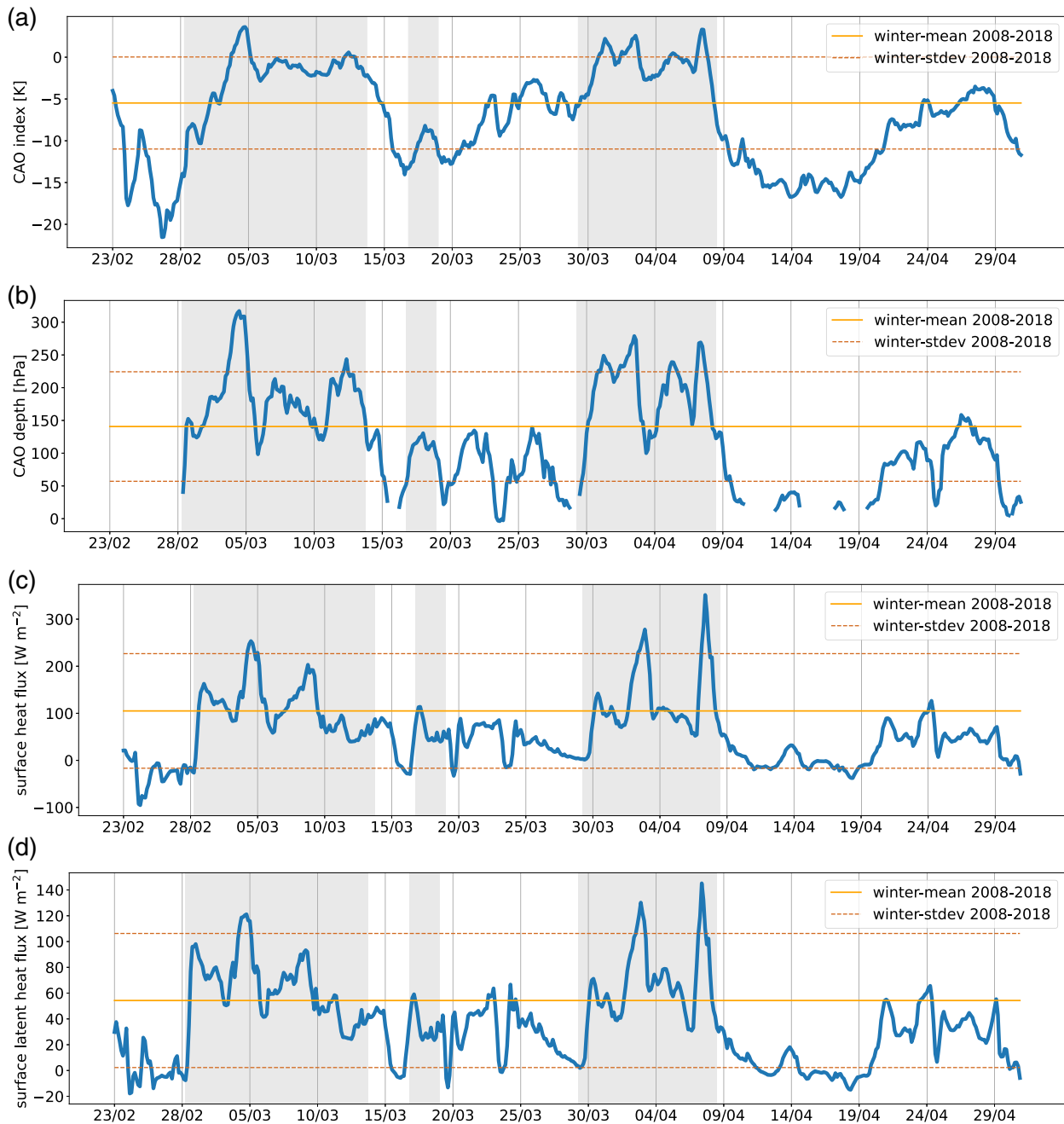
FIGURE 3 Cold-air outbreak metrics for the Iceland Sea showing (a) a cold-air outbreak (CAO) index $= \theta_{SST} - \theta_{800}$, where the subscript indicates the level as 800 hPa, (b) the CAO depth, defined as the height in hPa where $\theta = \theta_{SST}$, (c) the surface sensible heat flux, and (d) the surface latent heat flux. The time series are area-averaged over a 100-km circle centred at 70° N, 16° W from 23 February to 1 May 2018 using ERA5 output. The extended winter (November–March) mean and ± 1 standard deviation from 2008 to 2018 are shown as amber lines. Three periods of CAO are shown via shading: The first and longest (0600 UTC 28 February to 1800 UTC 13 March) is the main focus of this study. Two subsequent CAO periods are also indicated: from 1800 UTC 16 March to 0000 UTC 19 March which has more impact on the Greenland and Norwegian seas; and from 0600 UTC 29 March to 1200 UTC 8 April which is discussed briefly in Section 5 [Colour figure can be viewed at wileyonlinelibrary.com]

change in surface heat flux forcing as the CAO strengths between 1 and 4 March.

The ABL structure of the CAO event is corroborated by 'snapshot' cross-sections based on aircraft observations.

In a cross-section heading south from the research vessel on 1 March, θ and RH are relatively constant over a distance of approximately 200 km, while the ABL increases in height from around 600 to 1,000 m; the turbulent SHFs
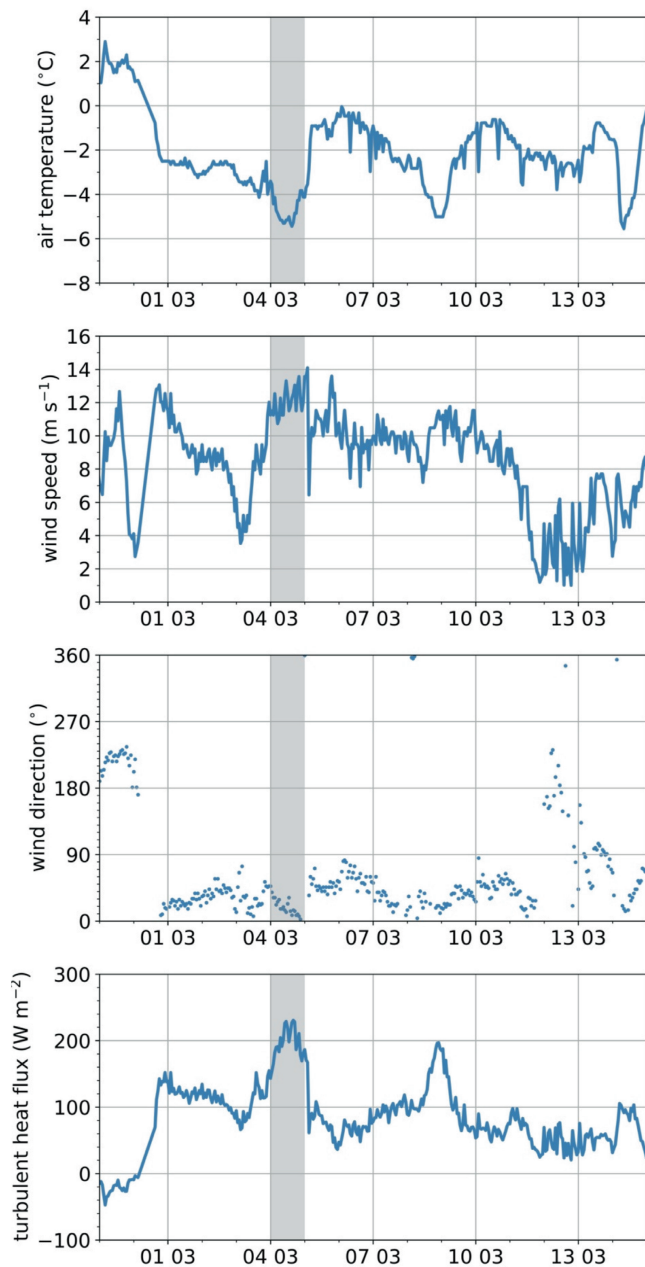
FIGURE 4 Observations from the meteorological buoy in the NW Iceland Sea showing air temperature, 10-m wind speed, wind direction, and total turbulent heat flux (as indicated). The period shown includes the cold-air outbreak (CAO) from 0600 UTC 28 February to 1800 UTC 13 March 2018, with the CAO peak on 4 March shaded [Colour figure can be viewed at wileyonlinelibrary.com]

4 and 6 March illustrate a similar story (not shown). The observed thermodynamic structure of the CAO event is qualitatively consistent with aircraft-based snapshots of other CAOs sampled by aircraft over the subpolar seas (e.g., Brümmer, 1996; Renfrew and Moore, 1999).

The spatial structure of the CAO event is also illustrated in Figure 7 using surface-layer observations at the onset (1 March) and peak (4 March). In general, these aircraft- and ship-based observations correspond well to each other (allowing for some discrepancies due to time, such as the decrease in θ between the two flights on 1 March). The air is 1–2 K colder to the west, closer to the sea-ice edge, on both days as well as over the tongue of sea ice at approximately 70° N on 1 March. There is a similar west-to-east gradient in surface temperature and heat fluxes (not shown). Overall, aside from gradients related to the proximity to the sea ice, the CAO is reasonably homogeneous in θ, RH, winds, and turbulent fluxes over a distance of up to approximately 200 km. This implies the mesoscale spatial character of such CAO events should be relatively straightforward to simulate in suitable numerical models.

Compared to 1 March, the CAO is uniformly colder and windier on 4 March, consistent with the event reaching its peak then; Figure 7 provides a spatial illustration of the time series in Figures 3–5. The CAO development, from 1 to 4 March, is also illustrated via vertical profiles of mean and turbulent quantities from coincident aircraft and ship flux-runs (Figure 8). The strengthening of the CAO is associated with an ABL increase in wind speed of 5–10 m·s^{-1}, a decrease in θ of about 4 K, an increase in momentum flux of 0.1–0.5 N^{-2}, and an increase in SHF of 100–150 W·m^{-2}. These changes are predominantly temporal, that is, related to a strengthening of the CAO. In contrast, the RH and LHF profiles are not significantly different. The flux-run profiles of θ and wind speed are relatively constant with height, while the RH increases with height, corroborating the cross-sections (e.g., Figures 5, 6). On 4 March, the momentum flux and SHF are higher at all heights, while the LHF is confined between −26 and 38 W·m^{-2} above the surface layer, with notably low values between 80 and 160 m. On these legs the aircraft was flying in a subcloud environment with RH over 85%, which likely limited the LHF. The flights were below a dense low-level cloud layer, with cloud droplet numbers measured at 300 cm^{-3} and a cloud base of about 250 m altitude. The ABL was replete with shallow convection and the low LHFs may be partly due to upward and downward moisture fluxes balancing each other. A pronounced decrease in SHF and LHF with height has been seen in other CAO case studies (e.g., Bane Jr and Osgood, 1989; Grossman and Betts, 1990; Brümmer, 1999).

are confined to between ±40 W·m^{-2} with higher values associated with a rise in ABL height (Figure 6). In a west–east cross-section passing over the *Alliance*, the ABL increases from around 600 to 800 m (over 150 km from the MIZ offshore) with turbulent SHF observations peaking at 80 W·m^{-2} at the ice edge (see Figure 8 in Renfrew *et al.*, 2019). Aircraft-based cross-sections for

FIGURE 5 Time–height cross-section for the first part of the cold-air outbreak (CAO) from radiosonde profiles in the Iceland Sea, showing: (a) potential temperature; (b) relative humidity; and (c) wind speed. In (a) every fifth contour (or 5 K) is bold. Triangles on the top axis mark the time of radiosonde releases. Note the profiles are from a relatively small 'survey' region (see Figure 1 for locations) meaning the variability illustrated here is predominantly temporal [Colour figure can be viewed at wileyonlinelibrary.com]
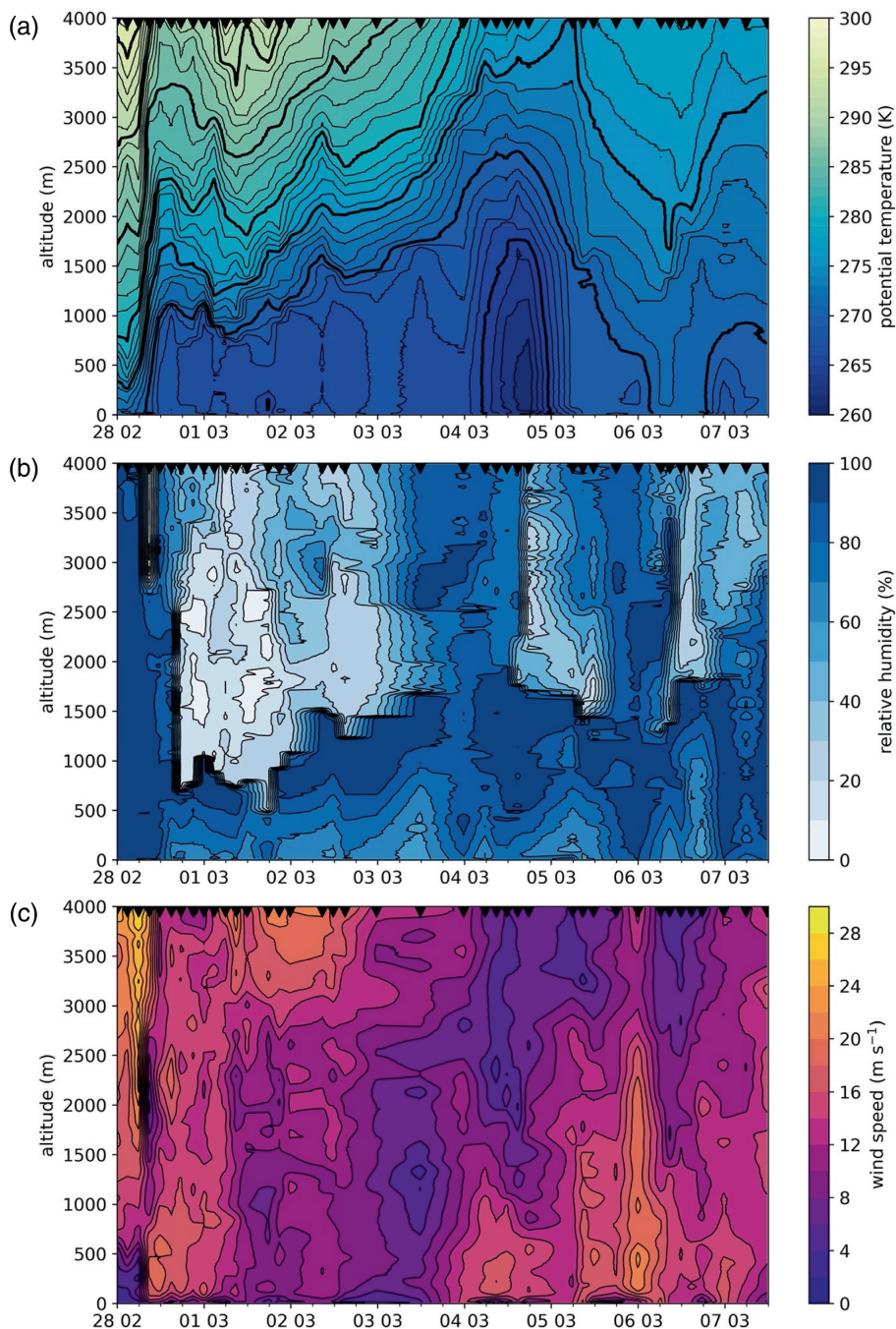
3.3 | One-dimensional energy conservation analysis

The vertical profiles of turbulent fluxes imply significant heat and water vapor convergence into the ABL driven by high surface fluxes (Figure 8). On synoptic timescales, it is cold-air advection that is driving these higher surface heat fluxes. However, changes on shorter timescales in the ABL structure, such as the variability seen in the radiosonde cross-section, can be attributed to local processes. For example, we examined quasi-Lagrangian radiosonde profiles from the beginning of the CAO event (at 1145 and

1500 UTC on 28 February) and found an increase in ABL height from 1,000 to 1,150 m, when surface-layer observations show no discernible change in temperature at the research vessel's location. This justifies neglecting horizontal processes and employing a 1D energy conservation analysis. Using the 1D mixed-layer model of Renfrew and King (2000) – their equation 6 and assuming entrainment at the ABL top is 10% of the surface flux – we find this 150-m increase in ABL height can be attributed to a convergence of turbulent sensible heat fluxes into the boundary layer. In short, larger-scale horizontal drivers and smaller-scale vertical processes are both important in
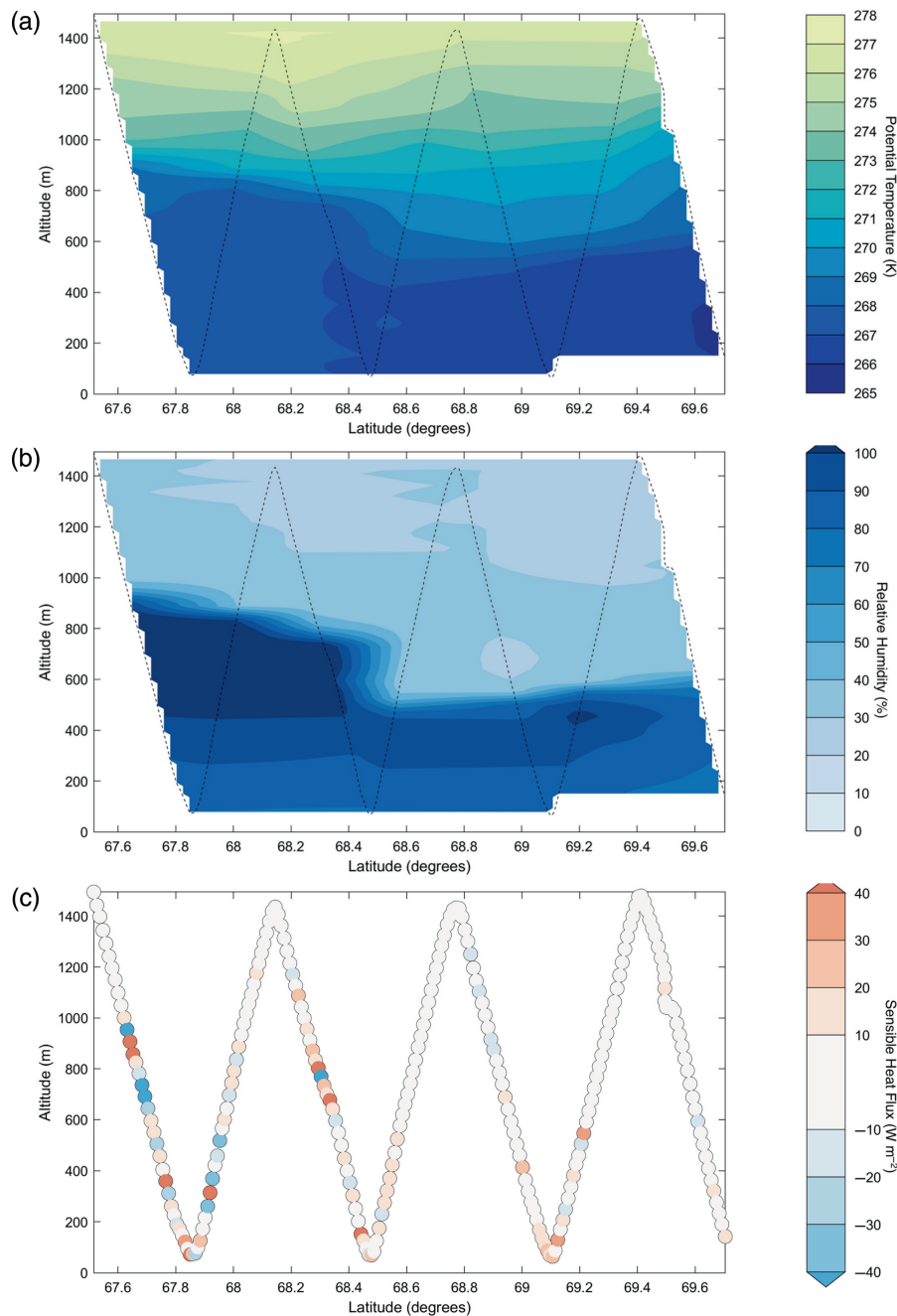
FIGURE 6 Cross-section of the atmospheric boundary layer (ABL) on 1 March 2018 from aircraft observations on flight 293 showing (a) potential temperature (K), (b) relative humidity with respect to ice from the LICOR instrument (%), and (c) sensible heat flux (W·m^{-2}). Please see Figure 1 for location. [Colour figure can be viewed at wileyonlinelibrary.com]

the evolution of this CAO event; in the next section, we examine whether the same is true in the response of the ocean.

4 | IMPACTS ON THE OCEAN MIXED LAYER

4.1 | Observational strategy

Based on our CAO forecasts, the research vessel transited to the western Iceland Sea and conducted a rapid XCTD survey offshore of the MIZ to characterize the state of the

ocean before the CAO event. Over the following eight days of the CAO event, the ship performed two 'triangle surveys' (see Figure 1). The rationale was to sample two control volumes (a northern one and a southern one) to assess the relative importance of air-sea fluxes versus advection in dictating the evolution of the ocean mixed layer. The east–west base of each triangle was sampled with CTDs, while XCTDs were used for the two sides to sample as synoptically as possible. Unfortunately, the quality of the shipboard acoustic Doppler current profiler (ADCP) data was significantly degraded while the ship was steaming (something which did not become clear until after the cruise), making it impossible to evaluate the intended control
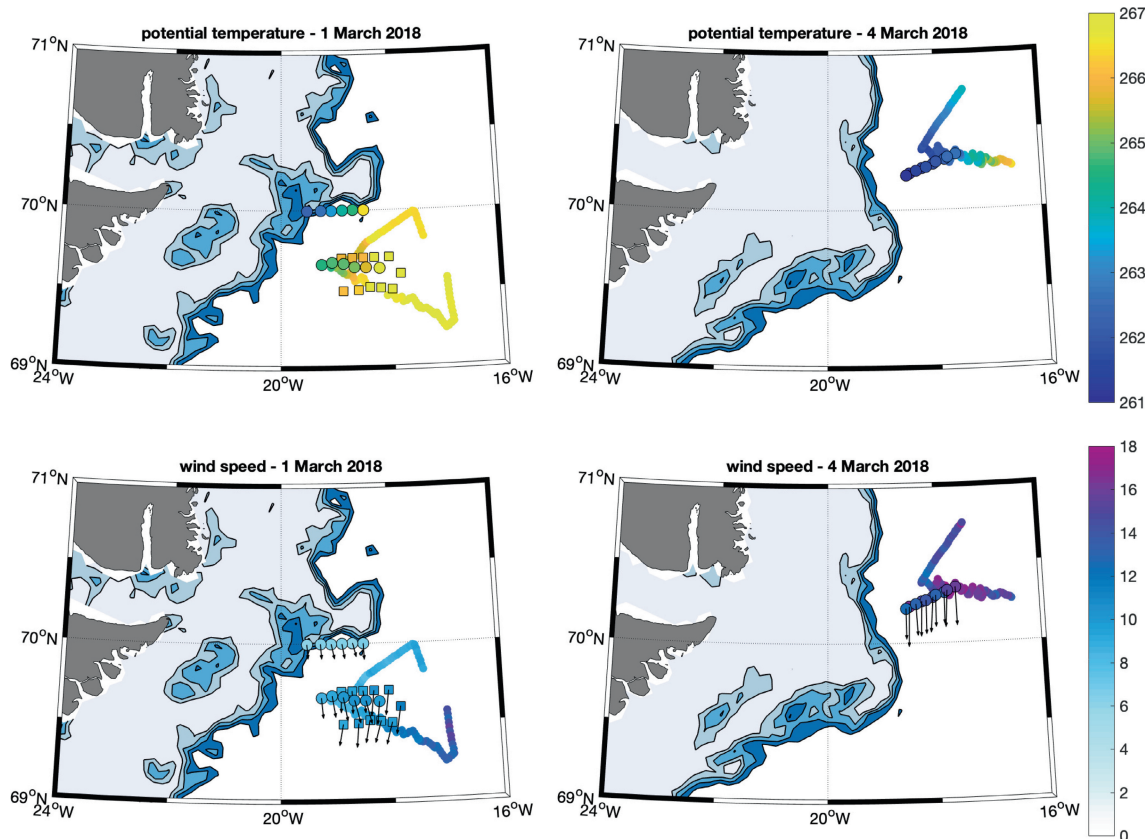
FIGURE 7 Surface-layer observations at the onset (1 March; left column) and the peak (4 March; right column) of the cold-air outbreak (CAO). The top panels show potential temperature (K) and bottom panels show wind speed (m·s^{-1}). The aircraft observations are run averages on 1 March (flight 293 at ~35 m altitude between 1028 and 1059 UTC, squares; flight 294 at ~50 m between 1517 and 1633 UTC, circles) and on 4 March (flight 295 at ~80 and ~90 m between 1240 and 1307 UTC, circles). The ship-based observations (small circles) are ten-minute averages from 20 to 40 m for the entirety of each day as the ship progressed clockwise around the southern survey triangle (left column) or northern survey triangle (right column). For clarity, wind vectors are only shown for the aircraft data. Sea-ice fraction is shown via shaded contours from 0.2 to 0.8 (based on Advanced Microwave Scanning Radiometer 2 [AMSR2] data) [Colour figure can be viewed at wileyonlinelibrary.com]

volume calculations accurately. A series of XBT transects were then carried out before the *Alliance* headed south on 8 March. In addition to the research vessel measurements, an Argo float, glider, and mooring also collected hydrographic data during the CAO (see Section 2.2; Figure 1). During the CAO event the glider was programmed to sample in 'mooring mode', conducting dives near the 1,500 m isobath on the continental slope. The locations of all of these ocean measurements are shown in Figure 9.

4.2 | Mixed layer bulk response

The mixed-layer (ML) properties of temperature, salinity, density, and depth were determined using the multi-step procedure of Pickart *et al.* (2002). We applied this procedure to all of the hydrographic profiles collected, except those from the mooring measurements due to their high temporal resolution. For the mooring dataset an

automated routine was employed that determines the depth above which the linear fit through all discrete temperature measurements up to the surface best matches a constant temperature profile. Figure 9 shows the spatial distribution of ML potential density and depth during the event; time-averaged values are shown for locations with repeat sampling. The mixed layers are less dense (26–27.92 kg·m^{-3}) and shallower (10–100 m) in the boundary current region, where the water column was highly stratified and light Polar Surface Water occupied the near-surface layer (Huang *et al.*, 2021). In contrast, the mixed layers are denser (27.92–28.0 kg·m^{-3}) and deeper (100–250 m) seaward of 18–16º W – towards the interior of the Iceland Sea. Notably, the ML characteristics from the different platforms are consistent. The distinction in ML properties appears related to proximity to the continental slope and the East Greenland Current. It suggests a divide into two regimes: a boundary regime where the mixed layer is shallower and lighter, and an interior regime where
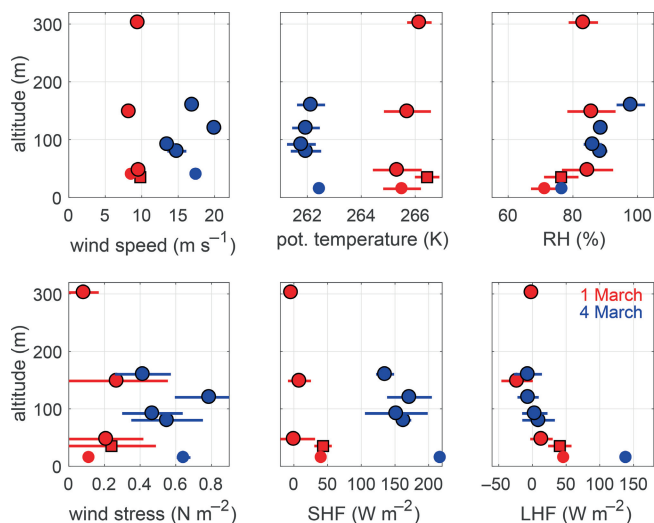
FIGURE 8 Atmospheric boundary-layer variables from the onset (1 March; red) and peak (4 March; blue) of the cold-air outbreak (CAO). The mean (symbol) and standard deviation (line) are from flux runs of 2.5 min from aircraft observations (flight 293, squares; flights 294 and 295, circles); and from 10-min runs from the ship-based observations (smaller circles without outline) for the same time window. Only runs from the southern leg of flight 294 are used, as the northern leg was over the marginal ice zone (see Figure 7). Panels show wind speed, potential temperature, relative humidity (RH), wind stress, sensible heat flux (SHF); and latent heat flux (LHF) versus altitude. Note that the aircraft fluxes are from eddy covariance estimates, while the ship fluxes are from the COARE bulk algorithm [Colour figure can be viewed at wileyonlinelibrary.com]

the mixed layer is deeper and denser. The black line in Figure 9 delineates these two regimes and approximately coincides with the extent of the East Greenland Current (EGC) (see Figures 7 and 10 of Huang *et al.*, 2021). Such a division is supported by an analysis of the full six-week *Alliance* hydrographic dataset by Huang *et al.* (2021), who identified regional differences of wintertime water mass transformation in the boundary current versus interior regions of the western Iceland and Greenland Seas. In the boundary current region, they found significant variability in ML properties, while in the interior there was a more consistent production of dense water via diapycnal processes.

We analyse the ocean response to the CAO distinguished into these boundary and interior regimes, as denoted in Figure 9. While the mixed layers sampled by the glider were clearly in the boundary regime, the mixed layers sampled by the mooring and Argo float were near the transition between the two regimes and so are considered separately below. The ocean response to the CAO is investigated by comparing the change in ML properties between two stages of the CAO: (i) the pre- and early-CAO period, from 0000 UTC 27 February to 1200 UTC 4 March; and (ii) the late-CAO period, from 1200 UTC 4 March to 0000

UTC 8 March. By compiling our ML observations into two regimes and two time periods, we can average out some of the inherent variability.

In both the boundary and interior regimes, a modest deepening of the mixed layer was observed from the early to late period of the CAO (Figure 10; Table I). The boundary regime ML depth increased from 41 ± 3 to 55 ± 10 m, while the interior regime ML depth increased from 131 ± 8 to 152 ± 11 m, where the mean $\pm$ standard errors are given. This ML deepening partly stems from the significant increase in wind stress during this period (e.g., Figure 8). The response to the CAO was different for the ML temperature: in the boundary regime the mixed layer warmed by 0.15 ± 0.14°C, despite the heat loss from the ocean to the atmosphere, while in the interior regime it cooled by -0.05 ± 0.03°C. With regard to ML salinity, the boundary regime became saltier by 0.179 ± 0.057, much more than in the interior regime which increased by only 0.007 ± 0.005. A statistical analysis (Table I) shows that when all the observation types are averaged, the difference in the means generally exceeds the standard error implying significance by this measure; while a Welch's unequal variances *t*-test shows *p* values below 0.15 for salinity and ML depth in the boundary region and temperature, salinity and ML depth in the interior region. Given this is a single case study of a highly variable region, the differences in the ocean are clearly important.

What is the reason for this differing response in ML properties between the two regimes? By comparing vertical sections of temperature and salinity at different stages of the CAO, Huang *et al.* (2021) demonstrated that the cold and fresh Polar Surface Water in the boundary regime was advected onshore by Ekman transport under the strong northerly wind during the event. In concert with this warm and salty Atlantic-origin water was fluxed laterally offshore by turbulent mixing. This resulted in a short-term warming and salinification of the mixed layer. Our results corroborate this interpretation. Furthermore, our observations indicate that, in the interior regime, surface cooling dominated the response with less influence from lateral effects. (We note that isolated eddies shed from the boundary current can modulate the ML response in the interior Iceland and Greenland Seas, as demonstrated by Huang *et al.*, 2021.)

The mooring was located on the southern slope of the Eggvin Offset (Figure 1), a passage between the Kolbeinsey and West Jan Mayen Ridges that connects the boundary current region to the interior Iceland Sea. During the CAO, the mean ML depths in the Offset were in between those of the boundary and interior regimes (Figure 10, yellow symbols). The mean mixed layers became slightly deeper, colder, and saltier during the CAO, qualitatively similar to the interior regime. However, the overall changes were
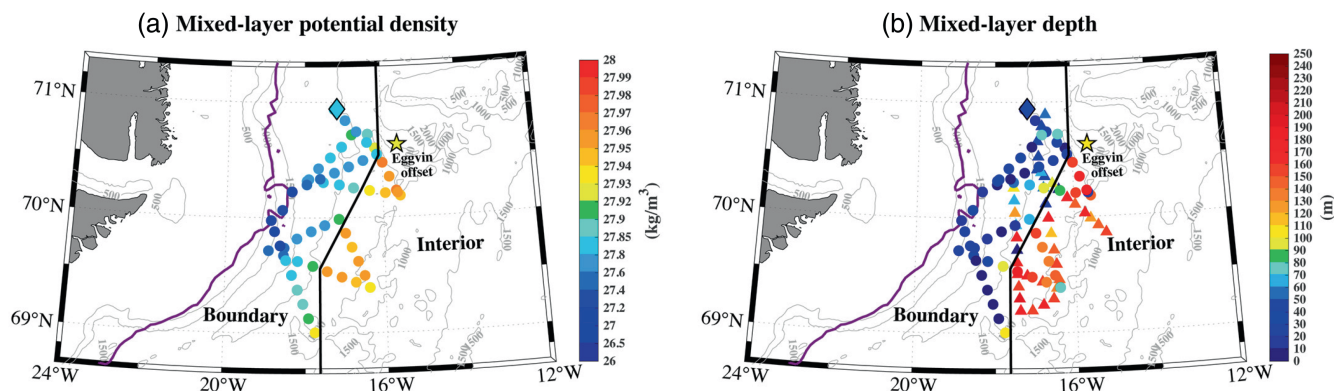
FIGURE 9 Observations of the ocean mixed layer showing (a) potential density and (b) mixed-layer depth between 27 February and 8 March 2018, encompassing the first part of the cold-air outbreak (CAO). Observations are from conductivity–temperature-depth systems (CTDs) and expendable CTDs (XCTDs) (circles) and bathythermographs (XBTs) (triangles), the mooring (star) and a glider (diamond). The sampling sites can be divided into interior and boundary current locations, separated by the black line, based on the mixed-layer properties shown. The mooring location, in the Eggvin offset, is an area of complex bathymetry and within the transition between the interior and boundary regions. The mean sea-ice cover is indicated by the 0.2 sea-ice fraction over this period from Advanced Microwave Scanning Radiometer 2 (AMSR2) data (purple line). The bathymetry is shown as grey contours (from ETOPO1). By convention a potential density of 1,028 kg·m^{-3} is denoted as 28 kg·m^{-3} [Colour figure can be viewed at wileyonlinelibrary.com]
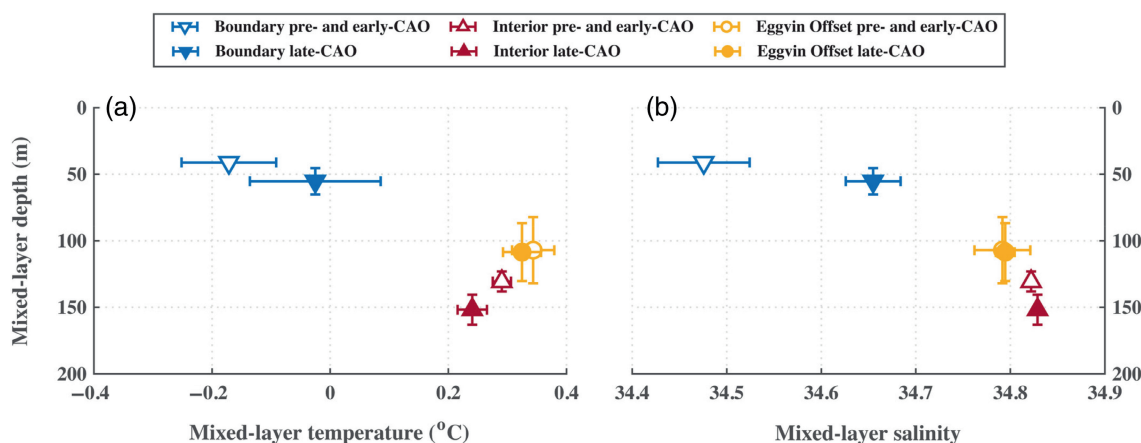

FIGURE 10 Ocean mixed-layer properties divided by location–boundary current (blue), interior (red) and the Eggvin offset (yellow); as well as time – early cold-air outbreak (CAO) (open symbols) and late-CAO (filled symbols). Panel (a) shows mixed-layer temperature versus depth; panel (b) shows mixed-layer salinity versus depth. In each case, the average and standard error are shown. The pre- and early-CAO period is from 0000 UTC 27 February to 1200 UTC 4 March; the late-CAO period is from 1200 UTC 4 March to 0000 UTC 8 March. Observations are from a combination of profiles from conductivity–temperature-depth systems (CTDs), extendable CTDs (XCTDs), bathythermographs (XBTs), and the glider (triangles) and from the mooring (circles) – also see Table I [Colour figure can be viewed at wileyonlinelibrary.com]

very small and, when compared to the standard error, not statistically significant. We hypothesise that this muted response is due to the effect of lateral advection. The mean flow at the mooring site was eastward, which is consistent with the expectations of geostrophic flow through the the Eggvin Offset. As such, warm and saline Atlantic-origin water, likely originating from the boundary, must have had considerable influence on the stratification and convection at this location, dampening the effects of the CAO.

A spatial picture of the surface response of the ocean to the CAO event can be seen from satellite-based SST

analyses (Figure 11). After the early-CAO period, there is generally a modest cooling of the sea surface of the western Iceland and Greenland Seas, although there are patches of warming, including at the mooring location. After the late-CAO period, there is a widespread and pronounced SST cooling (up to −2°C) covering most of the Iceland Sea region. However, the cooling is still patchy. In particular, there are regions of up to 1–2°C warming along the sea-ice edge – approximately following the path of the East Greenland Current – and in the northern Denmark Strait. Some of these patches reflect changes in the distribution

TABLE I Measurements from different regions of the Iceland Sea showing the number of profiles and the *difference* in ML properties between the late and early cold-air outbreak (CAO) periods

Region	Measurement platform	No. of profiles: Early/late-CAO	Mean difference ± standard error for:		
			ML temperature (°C)	ML salinity	ML depth (m)
Boundary	CTD	11/6	0.16 ± 0.34	**0.215 ± 0.151**	**31 ± 27**
	XCTD	32/14	0.08 ± 0.19	**0.224 ± 0.077**	1 ± 10
	XBT	13/11	**0.38 ± 0.38**	-	**37 ± 30**
	Glider	25/40	-0.03 ± 0.04	**0.098 ± 0.008**	**-13 ± 5**
	All	81/71	**0.15 ± 0.14**	**0.179 ± 0.057**	**14 ± 10**
			$p = 0.224$	$p = 0.003$	$p = 0.149$
Interior	CTD	12/7	**-0.05 ± 0.05**	0.004 ± 0.007	10 ± 28
	XCTD	8/8	-0.01 ± 0.06	**0.010 ± 0.005**	18 ± 24
	XBT	9/6	**-0.10 ± 0.05**	-	**36 ± 17**
	All	29/21	**-0.05 ± 0.03**	**0.007 ± 0.004**	**21 ± 14**
			$p = 0.094$	$p = 0.088$	$p = 0.129$
Eggvin offset	Mooring	528/336	-0.02 ± 0.05	0.003 ± 0.031	1 ± 33

Note: The differences in ocean ML temperature, salinity and depth between the late- and early-CAO periods are calculated as ($\overline{\text{Mean}_{\text{late–CAO}}} - \overline{\text{Mean}_{\text{early–CAO}}}$). An uncertainty estimate is provided by the standard error, estimated using standard errors of the early- and late-CAO properties ($S = \sqrt{S_{\text{early–CAO}}^2 + S_{\text{late–CAO}}^2}$), where S is the standard deviation of the sample/$\sqrt{(n-2)}$. Two measures of significance are provided: (i) the values are bold when the mean difference is greater than the standard error; and (ii) a significance (p value) is given using Welch's t-test for the mean difference between the early and late-CAO period. Note differences between the handful of hydrographic profiles in the Eggvin Offset from the Argo float are not shown; differences between the large number of mooring measurements are more statistically robust.

of sea ice and associated colder surface waters, but some appear to reflect other processes such as the upward mixing of warmer subsurface Atlantic-origin waters, or lateral advection from eddies. Numerous eddies were observed in the hydrographic data (Huang *et al.*, 2021) and these are known to be an important vehicle for heat transport in such marginal seas (Spall, 2011).

A temporal picture of the ML response to the CAO event is presented in Figure 12 using observations from the mooring and the Argo float (both in the Eggvin Offset at this time). There is substantial variability in ML depth, temperature, and salinity during the CAO. The surface THFs show a continuous upward heat flux with maxima on 4 and 9 March. The co-located high-frequency mooring observations show periods of ML cooling and deepening (e.g., 1, 3–4, 8 and 12 March); as well as periods of ML warming (e.g., 6 and 11 March) and shoaling (e.g., 3, 6 and 10 March) which cannot be explained by the direct atmospheric forcing. The Argo float observations broadly corroborate the mooring timeseries for ML temperature and depth, and also illustrate substantial changes in ML salinity (e.g., in the mixed layer on 2–3 March). The warmer mixed layers seen in both timeseries generally coincide with convection penetrating into the subsurface Atlantic-origin water (centred at a depth of 200–300 m)

and mixing up warmer water. However, the rapid shoaling of the mixed layer also points to the importance of lateral advection and eddies in this region – something not immediately apparent when looking at mean ML changes (cf. Figure 10). At the Eggvin Offset, the complex bathymetry results in a finely balanced competition between a direct cooling and deepening response to the atmospheric forcing and lateral advection.

4.3 | One-dimensional model simulation

To help understand the underlying mechanisms regulating the response of the ocean to the CAO, a one-dimensional ML model was employed. The Price–Weller–Pinkel (PWP) model parameterizes mixing from heat and momentum fluxes imposed at the ocean surface and the entrainment of stratified fluid from below, as described in Price *et al.* (1986). It has previously been successfully used to simulate changes in ML properties in the western Nordic Seas (e.g., Moore *et al.*, 2015; Våge *et al.*, 2018; Brakstad *et al.*, 2019; Huang *et al.*, 2021). Here we use CTD profiles from the base of both survey triangles during the pre- and early-CAO period as initial conditions, and apply atmospheric forcing from ERA5. Reanalysis
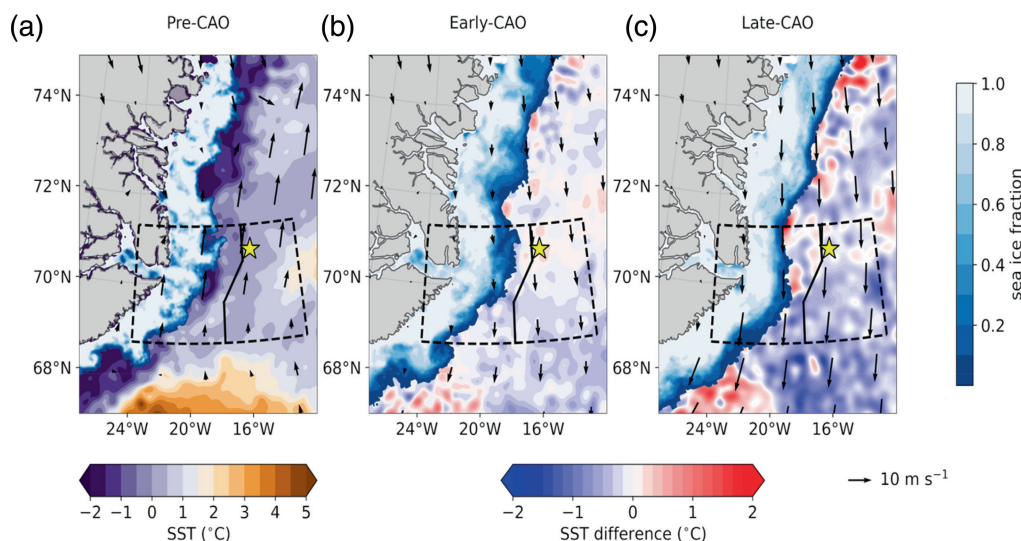
FIGURE 11   Spatial maps of sea surface temperature and the change in SST. Panel (a) shows SST immediately before the cold-air outbreak (pre-CAO) on 27 February 2018. Panels (b) and (c) show the difference between the early- and late-CAO periods and 27 February. The early-CAO and late-CAO periods are defined following Figure 10. The SST fields are from the OSTIA product, sea-ice fractions are from the Advanced Microwave Scanning Radiometer 2 (AMSR2), and the 10-m wind vectors are from ERA5. The location of the meteorological buoy and mooring is shown by the star. The domain of Figure 9 and the divide between the boundary and interior regions is overlain in black [Colour figure can be viewed at wileyonlinelibrary.com]

fluxes are used (in preference to estimates from the buoy observations) to enable a matching to the location of the CTD stations. Previous work has demonstrated ERA5 does not have any significant biases and is relatively accurate over open water in this region (Renfrew *et al.*, 2021). The model was run from the pre- and early-CAO period to the late-CAO period with the simulated profiles compared to observations.

For the interior regime, the PWP model successfully reproduces the evolution of ML density during the CAO event, that is, a densification in the upper 150 m of the water column (Figure 13). This densification is caused by a ML cooling of about 0.1°C and a small increase in salinity of 0.004. On average the PWP model overestimates the cooling and underestimates the salinification, with these errors compensating to produce an accurate density profile. The simulations demonstrate that, for the interior regime, vertical processes dominate and the small biases evident are likely associated with (unrepresented) weak lateral mixing of warm and salty Atlantic-origin water into the interior (see Figures 5 and 13 of Huang *et al.*, 2021).

For the boundary regime, the PWP model is less successful. The model simulates a ML cooling of 0.3°C and a small (0.05) increase in salinity (not shown), in contrast to the approximately 0.1°C of warming and the significant (0.2) increase in salinity that is observed (Figure 10). This implies that (unrepresented) lateral processes dominate over vertical processes in the boundary current region at this time. We have also applied the PWP model in the

Eggvin Offset. In particular, we used a pre-CAO Argo float profile and a pre-CAO CTD cast near the mooring as initial profiles and compared the model output to late-CAO profiles from the Argo float and mooring measurements respectively. In keeping with observations (Figure 10), the simulated mixed layer became colder and saltier, but the model did not reproduce the magnitude of the changes well – becoming too cold and fresh. This implies that lateral advection of warm and saline water substantially affects the ML evolution in this region too.

In short, the ML simulations demonstrate that, for the interior regime, air–sea vertical processes dominate the short-term ocean response to the CAO (i.e., surface fluxes and vertical mixing in the ocean); while, for the boundary regime, lateral processes dominate the short-term response.

5 | SEASONAL CONTEXT AND DISCUSSION

Our time series observations give us the opportunity to place the CAO event into a seasonal context. Figure 3 shows CAO metrics from February to April 2018 – the ocean convection season – and illustrates three CAO events: the event analysed in detail here, a very short event shortly thereafter, and a week-long event in early April. The second event, on 16–18 March, was observed by the research vessel as a strong CAO over the Greenland Sea
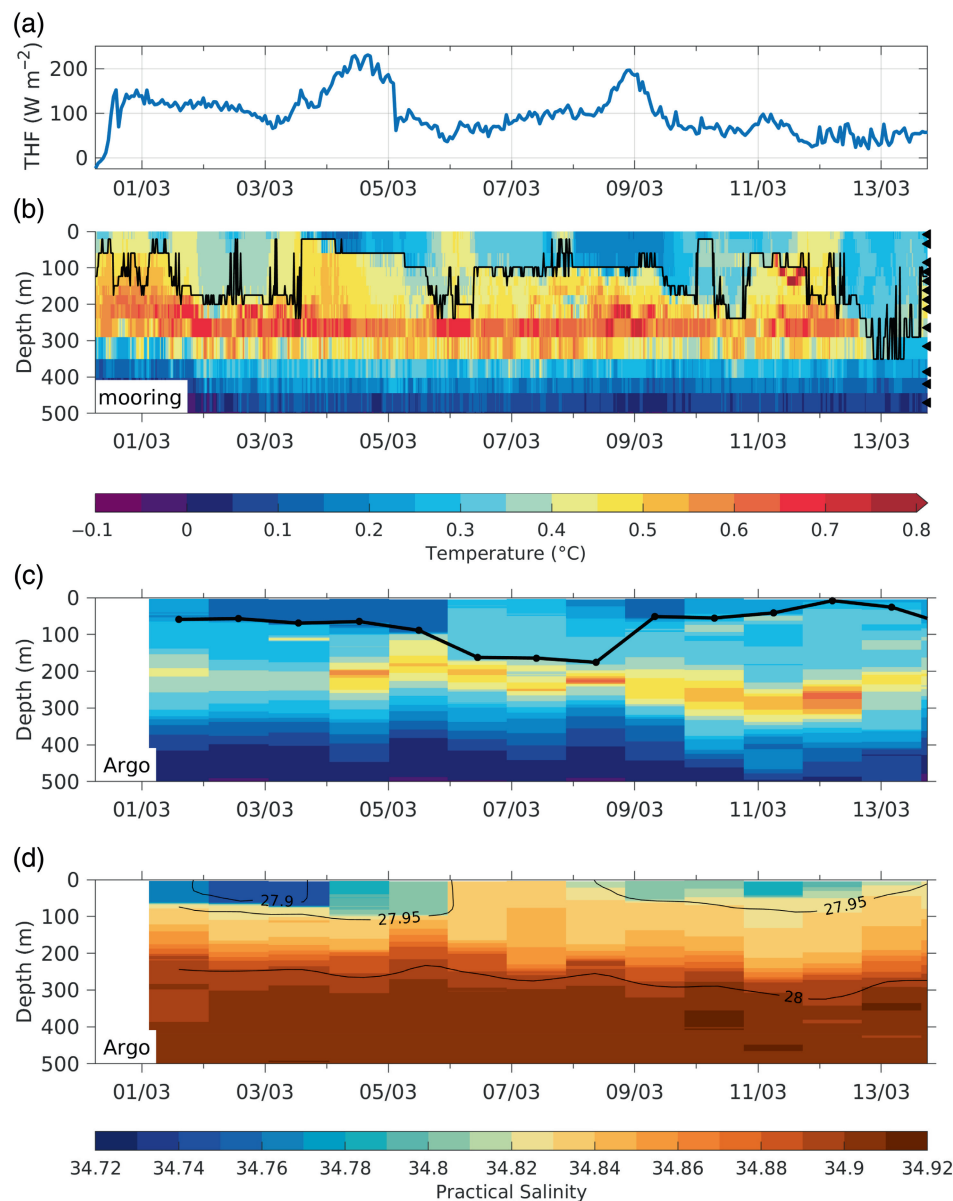
FIGURE 12 Time series of turbulent heat flux (THF) and time–depth cross-sections of upper ocean properties during the cold-air outbreak (CAO) from 0600 UTC 28 February to 1800 UTC 13 March 2018. Panel (a) shows the total THF from the meteorological buoy. Panels (b) and (c) show *in-situ* temperature and the mixed-layer depth (black line) from the Eggvin offset mooring and the Argo float respectively. Panel (d) shows salinity from the Argo float with isopycnals contoured in black [Colour figure can be viewed at wileyonlinelibrary.com]

with peak THF up to 470 W·m^{-2} and, based on radiosonde profiles, a similar thermodynamic structure to our case study (not shown). However, this event was weaker over the Iceland Sea. The observed THF at the buoy was only 100–150 W·m^{-2} and, responding to this, the mixed layer cooled and (after initially shoaling) deepened from approximately 20 to 150 m penetrating into and mixing with the relatively warm Atlantic-origin water below (Figure 14). Note that the presence of this Atlantic-origin water also varies, with relatively little present in mid-March, implying variability in its advection along this passage.

The third CAO event, from 28 March to 8 April, is stronger over the Iceland Sea at +1σ above the winter mean in the CAO index and CAO depth (Figure 3). CAO3 had northerly flow emanating from Fram Strait that swept a cold air mass across the Greenland, Norwegian, and Iceland Seas (not shown). Two large peaks in the reanalyses' surface heat fluxes are also evident in the buoy observations (Figures 3, 14), and were due to polar mesoscale cyclones (not shown). Based on radiosonde profiles from Jan Mayen, CAO3 had a qualitatively similar thermodynamic structure to that of the CAO case study analysed here (not shown). At the mooring site, CAO3 resulted in a strong cooling of the ocean mixed layer – in particular during the THF peak of 2–3 April – followed by a substantial deepening to 160 m (Figure 14). The mixed layer shoaled to 40 m on 6 April before deepening to 190 m following the second THF peak on 7 April. During the ML deepening periods the ML temperatures increased, likely from mixing with the warmer Atlantic-origin water underneath. This mixing up of warmer saltier water is also clear in the Argo float observations from the northern slope of
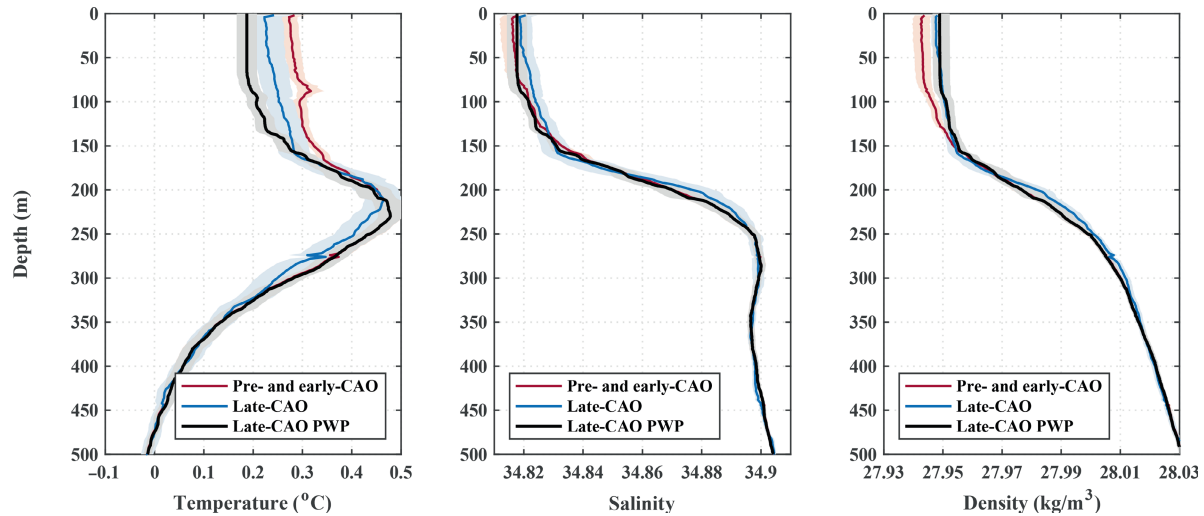
FIGURE 13 Observed oceanic profiles for the interior location from the pre- and early cold-air outbreak (CAO) (red) and late-CAO (blue) periods, along with the PWP model simulation showing the late-CAO period (black). Panels show temperature, salinity and density versus depth. For each period, the bold line indicates the mean and the shading depicts the range of profiles [Colour figure can be viewed at wileyonlinelibrary.com]

FIGURE 14 Time series of (a) total turbulent heat flux (THF) from the buoy and (b) upper ocean temperature and mixed-layer depth (black line) from the Eggvin offset mooring from 23 February to 1 May 2018. The periods of cold-air outbreak (CAO) are indicated by the grey shading in panel (a) [Colour figure can be viewed at wileyonlinelibrary.com]
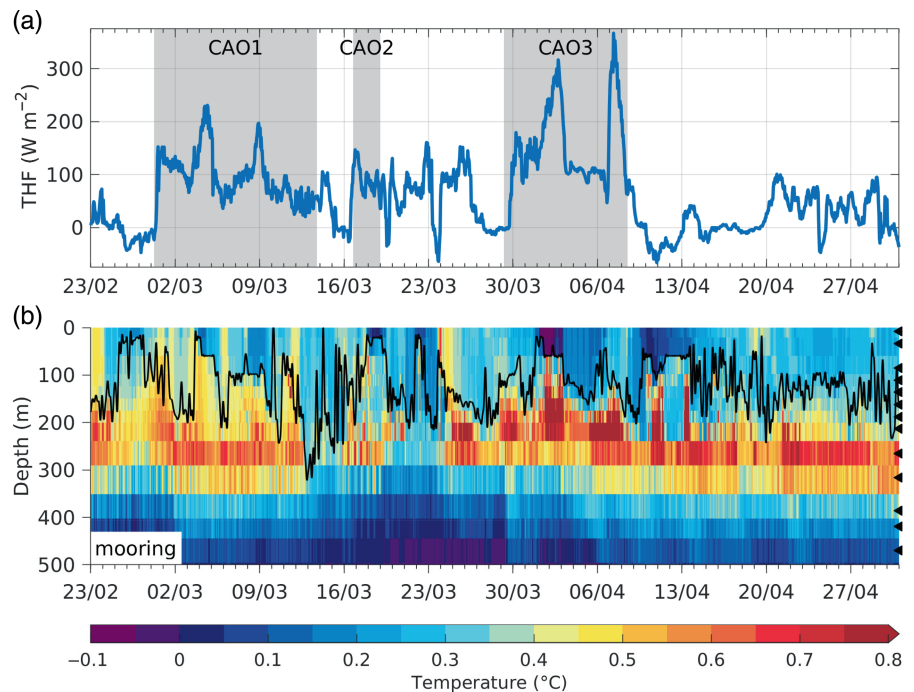
the Eggvin Offset at this time (not shown). These longer time series demonstrate that the mixed layer is highly variable, with rapid changes in ML depth, temperature, and salinity frequent and sometimes contrary to the atmospheric forcing. These findings reinforce those of Section 4; that at this location there is a finely balanced competition between atmospheric forcing and variable lateral advective processes in the evolution of the mixed layer.

Reviewing the entire season and comparing to previous work, the CAO presented here is a weak-to-moderate event that is typical of those occurring in the Iceland Sea (Figures 3, 14; Moore *et al.*, 2012; Harden *et al.*, 2015; Papritz and Spengler, 2017; Terpstra *et al.*, 2021). In this regard, we can interpret the short-term response of the ocean as typical for a CAO event in this region. However, the 2017/18 winter season was climatologically warm (see Renfrew *et al.*, 2019), so the ocean was not primed for water mass transformation. In colder years, it is likely that the same magnitude of CAO events would result in deeper mixed layers and that atmospheric forcing would be more

likely to win out over lateral advection over a larger region.

6 | CONCLUSIONS

Coupled *in-situ* observations of the atmosphere and ocean during a CAO over the Nordic Seas have allowed a detailed analysis of the event; Figure 15 is a summary schematic. The CAO is relatively homogeneous spatially, except for a gradient in near-surface meteorology and surface fluxes near the sea-ice edge, and well mixed in potential temperature and wind speed in the ABL. It evolves from a weak to a moderate-strength event, with peak surface heat fluxes of 220–350 $W \cdot m^{-2}$ over the northwest Iceland Sea. Local short-term fluctuations in the ABL structure can be explained by surface forcing; however, the broader evolution of the CAO is a result of synoptic scale forcing.
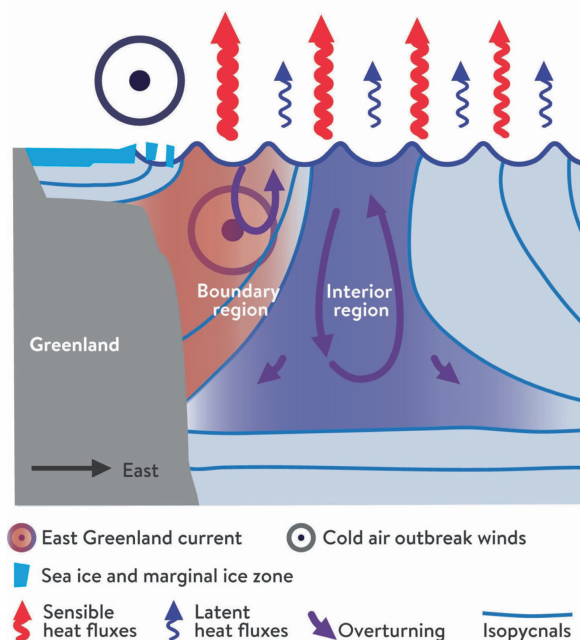
FIGURE 15 A schematic of the ocean mixed-layer response to this cold-air outbreak (CAO) event, illustrated via a cross-section of the Iceland Sea. In the boundary region there is a warming of the mixed layer (red shading), primarily due to the advection of relatively warm and salty water via the East Greenland Current (EGC); while in the interior region there is a cooling (blue shading), primarily due to surface heat loss into the atmosphere and an associated increase in mixed-layer density. This contributes to a deeper mixed layer in the interior region (that deepens further during the CAO, cf. Figure 10). In the atmospheric boundary layer (ABL), the sensible heat fluxes are larger than the latent heat fluxes, are highest close to the sea ice, and remain higher further into the ABL (cf. Figure 8) [Colour figure can be viewed at wileyonlinelibrary.com]

In the interior region of the Iceland Sea, the ocean mixed layer deepened, cooled, and slightly increased in salinity during the CAO, indicating that vertical processes dominate. However, in the boundary current region the mixed layer warmed and became significantly saltier due to a combination of lateral advection and entrainment of Atlantic-origin water from below. In the Eggvin Offset, where the mooring and buoy were located, there was a tightly fought competition between the atmospheric forcing and lateral advection leading to only a small mean ML deepening, cooling, and salinification in response to the CAO. Here, time series show high variability in ML properties throughout the CAO event, as well as during two subsequent CAO events. There is cooling and deepening of the mixed layer, but a supply of warmer Atlantic-origin water at 200–300 m depth means the mixed layer rapidly warms once convection penetrates to this depth, while lateral advection also leads to ML warming and shoaling. These results highlight the heterogenous ocean response to CAOs in the western Nordic Seas, where remarkably different water mass transformation processes can occur during any one event.

AUTHOR CONTRIBUTIONS
Ian A. Renfrew: Conceptualization; data curation; funding acquisition; investigation; visualization; writing – original draft; writing – review and editing. **Jie Huang:** Data curation; formal analysis; investigation; visualization; writing – original draft; writing – review and editing. **Stefanie Semper:** Data curation; investigation; visualization; writing – original draft; writing – review and editing. **Christopher Barrell:** Data curation; investigation; visualization; writing – review and editing. **Annick Terpstra:** Funding acquisition; investigation; visualization; writing – review and editing. **Robert Pickart:** Conceptualization; funding acquisition; investigation; writing – review and editing. **Kjetil Våge:** Conceptualization; funding acquisition; investigation; writing – review and editing. **Andrew Elvidge:** Data curation; visualization; writing – review and editing. **Thomas Spengler:** Writing – review and editing. **Anna-Marie Strehl:** Data curation; writing – review and editing. **Alexandra Weiss:** Data curation; writing – review and editing.

ORCID

Ian A. Renfrew https://orcid.org/0000-0001-9379-8215
Stefanie Semper https://orcid.org/0000-0003-1083-4642

REFERENCES

Abel, S.J., Boutle, I.A., Waite, K., Fox, S., Brown, P.R., Cotton, R., Lloyd, G., Choularton, T.W. and Bower, K.N. (2017) The role of precipitation in controlling the transition from stratocumulus to cumulus clouds in a northern hemisphere cold-air outbreak. *Journal of the Atmospheric Sciences*, 74, 2293–2314.

Atkinson, B.W. and Wu Zhang, J. (1996) Mesoscale shallow convection in the atmosphere. *Reviews of Geophysics*, 34, 403–431.

Bane, J.M., Jr. and Osgood, K.E. (1989) Wintime air-sea interaction processes across the Gulf stream. *Journal of Geophysical Research: Oceans*, 94, 10755–10772.

Brakstad, A., Våge, K., Håvik, L. and Moore, G.W.K. (2019) Water mass transformation in the Greenland Sea during the period 1986–2016. *J. Physical Oceanography*, 49, 121–140.

Brilouet, P.-E., Durand, P. and Canut, G. (2017) The marine atmospheric boundary layer under strong wind conditions: organized turbulence structure and flux estimates by airborne measurements. *J. Geophys. Res. Atmos.*, 122, 2115–2130. https://doi.org/10.1002/2016JD025960.

Brümmer, B. (1996) Boundary-layer modification in wintertime cold-air outbreaks from the Arctic Sea ice. *Boundary-Layer Meteorology*, 80, 109–125.

Brümmer, B. (1997) Boundary layer mass, water, and heat budgets in wintertime cold-air outbreaks from the Arctic Sea ice. *Monthly Weather Review*, 125, 1824–1837.

Brümmer, B. (1999) Roll and cell convection in wintertime Arctic cold-air outbreaks. *J. Atmospheric Sciences*, 56, 2613–2636.

Buckley, M.W. and Marshall, J. (2016) Observations, inferences, and mechanisms of the Atlantic meridional overturning circulation: a review. *Reviews of Geophysics*, 54, 5–63.

Chechin, D.G., Lüpkes, C., Repina, I.A. and Gryanik, V.M. (2013) Idealized dry quasi 2-D mesoscale simulations of cold-air outbreaks over the marginal sea ice zone with fine and coarse resolution. *Journal of Geophysical Research: Atmospheres*, 118, 8787–8813.

Chou, S.H. and Ferguson, M.P. (1991) Heat fluxes and roll circulations over the western gulf stream during an intense cold-air outbreak. *Boundary-Layer Meteorology*, 55, 255–281.

De Roode, S.R., Frederikse, T., Siebesma, A.P., Ackerman, A.S., Chylik, J., Field, P.R., Fricke, J., Gryschka, M., Hill, A., Honnert, R. and Krueger, S.K. (2019) Turbulent transport in the gray zone: a large Eddy model Intercomparison study of the CONSTRAIN cold air outbreak case. *Journal of Advances in Modeling Earth Systems*, 11, 597–623.

Duscha, C., Barrell, C., Renfrew, I.A., Brooks, I.M., Sodemann, H. and Reuder, J. (2022) A ship-based characterization of coherent boundary-layer structures over the lifecycle of a marine cold-air outbreak. *Boundary-Layer Meteorology*, 183, 355–380. https://doi.org/10.1007/s10546-022-00692-y.

Elvidge, A.D., Renfrew, I.A., Brooks, I.M., Srivastava, P., Yelland, M.J. and Prytherch, J. (2021) Surface heat and moisture exchange in the marginal ice zone: observations and a new parameterization scheme for weather and climate models. *J. Geophysical Research: Atmospheres*, 126, e2021JD034827. https://doi.org/10.1029/2021JD034827.

Elvidge, A.D., Renfrew, I.A., Weiss, A.I., Brooks, I.M., Lachlan-Cope, T.A. and King, J.C. (2016) Observations of surface momentum exchange over the marginal ice zone and recommendations for its parameterization. *Atmospheric Chemistry and Physics*, 16, 1545–1563. https://doi.org/10.5194/acp-16-1545-2016.

Fairall, C.W., Bradley, E.F., Hare, J.E., Grachev, A.A. and Edson, J.B. (2003) Bulk parameterization of air–sea fluxes: updates and verification for the COARE algorithm. *Journal of Climate*, 16, 571–591.

Fletcher, J., Mason, S. and Jakob, C. (2016) The climatology, meteorology, and boundary layer structure of marine cold air outbreaks in both hemispheres. *Journal of Climate*, 29, 1999–2014.

Geerts, B., Giangrande, S.E., McFarquhar, G.M., Xue, L., Abel, S.J., Comstock, J.M., Crewell, S., DeMott, P.J., Ebell, K., Field, P., Hill, T.C.J., Hunzinger, A., Jensen, M.P., Johnson, K.L., Juliano, T.W., Kollias, P., Kosovic, B., Lackner, C., Luke, E., Lüpkes, C., Matthews, A.A., Neggers, R., Ovchinnikov, M., Powers, H., Shupe, M.D., Spengler, T., Swanson, B.E., Tjernström, M., Theisen, A.K., Wales, N.A., Wang, Y., Wendisch, M. and Wu, P. (2022) The COMBLE campaign: a study of marine

boundary-layer clouds in Arctic cold-air outbreaks. *Bulletin of the American Meteorological Society*, 103, E1371–E1389. https://doi.org/10.1175/BAMS-D-21-0044.1.

Grossman, R.L. and Betts, A.K. (1990) Air–sea interaction during an extreme cold air outbreak from the eastern coast of the United States. *Monthly Weather Review*, 118, 324–342.

Gryschka, M., Drüe, C., Etling, D. and Raasch, S. (2008) On the influence of sea-ice inhomogeneities onto roll convection in cold-air outbreaks. *Geophysical Research Letters*, 35, L23804. https://doi.org/10.1029/2008GL035845.

Gulev, S.K. and Belyaev, K. (2012) Probability distribution characteristics for surface air–sea turbulent heat fluxes over the global ocean. *Journal of Climate*, 25, 184–206.

Harden, B.E., Renfrew, I.A. and Petersen, G.N. (2011) A climatology of wintertime barrier winds off Southeast Greenland. *Journal of Climate*, 24, 4701–4717. https://doi.org/10.1175/2011JCLI4113.1.

Harden, B.E., Renfrew, I.A. and Petersen, G.N. (2015) Meteorological buoy observations from the Central Iceland Sea. *Journal of Geophysical Research – Atmospheres*, 120, 3199–3208. https://doi.org/10.1002/2014JD022584.

Hersbach, H., Bell, B., Berrisford, P., Hirahara, S., Horányi, A., Muñoz-Sabater, J., Nicolas, J., Peubey, C., Radu, R., Schepers, D., Simmons, A., Soci, C., Abdalla, S., Abellan, X., Balsamo, G., Bechtold, P., Biavati, G., Bidlot, J., Bonavita, M., Chiara, G., Dahlgren, P., Dee, D., Diamantakis, M., Dragani, R., Flemming, J., Forbes, R., Fuentes, M., Geer, A., Haimberger, L., Healy, S., Hogan, R.J., Hólm, E., Janisková, M., Keeley, S., Laloyaux, P., Lopez, P., Lupu, C., Radnoti, G., Rosnay, P., Rozum, I., Vamborg, F., Villaume, S. and Thépaut, J.N. (2020) The ERA5 global reanalysis. *Quarterly Journal of the Royal Meteorological Society*, 146, 1999–2049. https://doi.org/10.1002/qj.3803.

Huang, J., Pickart, R.S., Bahr, F., McRaven, L.T. and Xu, F. (2021) Wintertime water mass transformation in the western Iceland and Greenland seas. *Journal of Geophysical Research*, 126, e2020JC016893. https://doi.org/10.1029/2020JC016893.

Huang, J., Pickart, R.S., Huang, R.X., Lin, P., Brakstad, A. and Xu, F. (2020) Sources and upstream pathways of the densest overflow water in the Nordic seas. *Nature Communications*, 11, 1–9.

Isachsen, P.E., Drivdal, M., Eastwood, S., Gusdal, Y., Noer, G. and Saetra, Ø. (2013) Observations of the ocean response to cold air outbreaks and polar lows over the Nordic seas. *Geophysical Research Letters*, 40, 3667–3671. https://doi.org/10.1002/grl.50705.

Iwasaki, T., Shoji, T., Kanno, Y., Sawada, M., Ujiie, M. and Takaya, K. (2014) Isentropic analysis of polar cold airmass streams in the northern hemispheric winter. *Journal of the Atmospheric Sciences*, 71, 2230–2243.

Jónsson and Valdimarsson. (2004) A new path for the Denmark Strait overflow water from the Iceland Sea to Denmark Strait. *Geophysical Research Letters*, 31, L03305. https://doi.org/10.1029/2003GL019214.

Kolstad, E.W., Bracegirdle, T.J. and Seierstad, I.A. (2009) Marine cold-air outbreaks in the North Atlantic: temporal distribution and associations with large-scale atmospheric circulation. *Climate Dynamics*, 33, 187–197.

Lilly, J.M., Rhines, P.B., Visbeck, M., Davis, R., Lazier, J.R., Schott, F. and Farmer, D. (1999) Observing deep convection in the Labrador Sea during winter 1994/95. *Journal of Physical Oceanography*, 29, 2065–2098.

Liu, A.Q., Moore, G.W.K., Tsuboki, K. and Renfrew, I.A. (2004) A high-resolution simulation of convective roll clouds during a cold-air outbreak. *Geophysical Research Letters*, 31, L03101. https://doi.org/10.1029/2003GL018530.

Liu, A.Q., Moore, G.W.K., Tsuboki, K. and Renfrew, I.A. (2006) The effect of the sea-ice zone on the development of boundary-layer roll clouds during cold-air outbreaks. *Boundary-Layer Meteorology*, 118, 557–581.

Michel, C., Terpstra, A. and Spengler, T. (2018) Polar mesoscale cyclone climatology for the Nordic seas based on ERA-Interim. *Journal of Climate*, 31, 2511–2532, https://doi.org/10.1175/JCLI-D-16-0890.1.

Moore, G.W.K., Renfrew, I.A. and Pickart, R.S. (2012) Spatial distribution of air-sea heat fluxes over the sub-polar North Atlantic Ocean. *Geophysical Research Letters*, 39, L18806. https://doi.org/10.1029/2012GL053097.

Moore, G.W.K., Våge, K., Pickart, R.S. and Renfrew, I.A. (2015) Decreasing intensity of open-ocean convection in the Greenland and Iceland seas. *Nature Climate Change*, 5, 877–882. https://doi.org/10.1038/nclimate2688.

Moore, G.W.K., Våge, K., Renfrew, I.A. and Pickart, R.S. (2022) Sea-ice retreat suggests re-organization of water mass transformation in the Nordic and Barents seas. *Nature Communications*, 13, 67. https://doi.org/10.1038/s41467-021-27641-6.

Oltmanns, M., Straneo, F., Moore, G.W.K. and Mernild, S.H. (2014) Strong downslope wind events in Ammassalik, Southeast Greenland. *Journal of Climate*, 27, 977–993.

Outten, S.D., Renfrew, I.A. and Petersen, G.N. (2009) An easterly tip jet off cape farewell, Greenland. Part II: simulations and dynamics. *Quarterly J. Royal Meteorological Society*, 135, 1934–1949.

Pagowski, M. and Moore, G.W.K. (2001) A numerical study of an extreme cold-air outbreak over the Labrador Sea: sea ice, air–sea interaction, and development of polar lows. *Monthly Weather Review*, 129, 47–72.

Papritz, L. and Grams, C.M. (2018) Linking low-frequency large-scale circulation patterns to cold air outbreak formation in the northeastern North Atlantic. *Geophysical Research Letters*, 45, 2542–2553. https://doi.org/10.1002/2017GL076921.

Papritz, L. and Spengler, T. (2017) A Lagrangian climatology of wintertime cold air outbreaks in the Irminger and Nordic seas and their role in shaping air–sea heat fluxes. *Journal of Climate*, 30, 2717–2737.

Petersen, G.N. and Renfrew, I.A. (2009) Aircraft-based observations of air-sea fluxes over Denmark Strait and the Irminger Sea during high wind speed conditions. *Quarterly Journal of the Royal Meteorological Society*, 135, 2030–2045.

Pickart, R.S., Torres, D.J. and Clarke, R.A. (2002) Hydrography of the Labrador Sea during active convection. *Journal of Physical Oceanography*, 32, 428–457.

Pithan, F., Svensson, G., Caballero, R., Chechin, D., Cronin, T.W., Ekman, A.M., Neggers, R., Shupe, M.D., Solomon, A., Tjernström, M. and Wendisch, M. (2018) Role of air-mass transformations in exchange between the Arctic and mid-latitudes. *Nature Geoscience*, 11, 805–812.

Price, J.F., Weller, R.A. and Pinkel, R. (1986) Diurnal cycling: observations and models of the upper ocean response to diurnal heating, cooling, and wind mixing. *Journal of Geophysical Research: Oceans*, 91, 8411–8427.

Renfrew, I.A. and King, J.C. (2000) A simple model of the convective internal boundary layer and its application to surface heat

flux estimates within polynyas. *Boundary-Layer Meteorology*, 94, 335–356.

Renfrew, I.A. and Moore, G.W.K. (1999) An extreme cold-air outbreak over the Labrador Sea: roll vortices and air–sea interaction. *Monthly Weather Review*, 127, 2379–2394.

Renfrew, I.A., Barrell, C., Elvidge, A.D., Brooke, J.K., Duscha, C., King, J.C., Kristiansen, J., Lachlan Cope, T., Moore, G.W.K., Pickart, R.S., Reuder, J., Sandu, I., Sergeev, D., Terpstra, A., Våge, K. and Weiss, A. (2021) An evaluation of surface meteorology and fluxes over the Iceland and Greenland seas in ERA5 reanalysis: the impact of sea ice distribution. *Quarterly J. Royal Meteorol. Soc.*, 147, 691–712. https://doi.org/10.1002/qj.3941.

Renfrew, I.A., Outten, S.D. and Moore, G.W.K. (2009) An easterly tip jet off cape farewell, Greenland. Part I: aircraft observations. *Quarterly J. Royal Meteorol. Soc.*, 135, 1919–1933.

Renfrew, I.A., Pickart, R.S., Våge, K., Moore, G.W.K., Bracegirdle, T.J., Elvidge, A.D., Jeansson, E., Lachlan-Cope, T., McRaven, L.T., Papritz, L., Reuder, J., Sodemann, H., Terpstra, A., Waterman, S., Valdimarsson, H., Weiss, A., Almansi, M., Bahr, F., Brakstad, A., Barrell, C., Brooke, J.K., Brooks, B.J., Brooks, I.M., Brooks, M.E., Bruvik, E.M., Duscha, C., Fer, I., Golid, H.M., Hallerstig, M., Hessevik, I., Huang, J., Houghton, L., Jónsson, S., Jonassen, M., Jackson, K., Kvalsund, K., Kolstad, E.W., Konstali, K., Kristiansen, J., Ladkin, R., Lin, P., Macrander, A., Mitchell, A., Olafsson, H., Pacini, A., Payne, C., Palmason, B., Pérez-Hernández, M.D., Peterson, A.K., Petersen, G.N., Pisareva, M.N., Pope, J.O., Seidl, A., Semper, S., Sergeev, D., Skjelsvik, S., Søiland, H., Smith, D., Spall, M.A., Spengler, T., Touzeau, A., Tupper, G., Weng, Y., Williams, K.D., Yang, X. and Zhou, S. (2019) The Iceland Greenland seas project. *Bulletin of the American Meteorological Society*, 100, 1795–1817. https://doi.org/10.1175/BAMS-D-18-0217.1.

Schott, F., Visbeck, M. and Fischer, J. (1993) Observations of vertical currents and convection in the Central Greenland Sea during the winter of 1988–1989. *Journal of Geophysical Research: Oceans*, 98, 14401–14421.

Semper, S., Våge, K., Pickart, R.S., Jónsson, S. and Valdimarsson, H. (2022) Evolution and transformation of the north Icelandic Irminger current along the North Iceland shelf. *Journal of Geophysical Research: Oceans*, 127, e2021JC017700. https://doi.org/10.1029/2021JC017700.

Semper, S., Våge, K., Pickart, R.S., Valdimarsson, H., Torres, D.J. and Jónsson, S. (2019) The emergence of the north Icelandic jet and its evolution from Northeast Iceland to Denmark Strait. *Journal of Physical Oceanography*, 49, 2499–2521.

Sergeev, D.E., Renfrew, I.A. and Spengler, T. (2018) Modification of polar low development by orography and sea ice. *Monthly Weather Review*, 146, 3325–3341. https://doi.org/10.1175/MWR-D-18-0086.1.

Sergeev, D.E., Renfrew, I.A., Spengler, T. and Dorling, S.R. (2017) Structure of a shear-line polar low. *Quarterly J. Royal Meteorol. Soc.*, 143, 12–26. https://doi.org/10.1002/qj.2911.

Skagseth, Ø., Eldevik, T., Årthun, M., Asbjørnsen, H., Lien, V.S. and Smedsrud, L.H. (2020) Reduced efficiency of the Barents Sea cooling machine. *Nature Climate Change*, 10, 661–666.

Spall, M.A. (2011) On the role of eddies and surface forcing in the heat transport and overturning circulation in marginal seas. *Journal of Climate*, 24, 4844–4858.

Spensberger, C. and Spengler, T. (2021) Sensitivity of Air-Sea heat exchange in cold-air outbreaks to model resolution and sea-ice distribution. *Journal of Geophysical Research: Atmospheres*, 126, 2020JD033610.

Spreen, G., Kaleschke, L. and Heygster, G. (2008) Sea ice remote sensing using AMSR-E 89 GHz channels. *J. Geophysical Research*, 113, C02S03. https://doi.org/10.1029/2005JC003384.

Steffen, E.L. and D'Asaro, E.A. (2002) Deep convection in the Labrador Sea as observed by Lagrangian floats. *Journal of Physical Oceanography*, 32, 475–492.

Swift, J.H. and Aagaard, K. (1981) Seasonal transitions and water mass formation in the Iceland and Greenland seas. *Deep Sea Research Part A. Oceanographic Research Papers*, 28, 1107–1129.

Swift, J.H., Aagaard, K. and Malmberg, S.-A. (1980) The contribution of the Denmark Strait overflow to the deep North Atlantic. *Deep Sea Research*, 27A, 29–42.

Sætra, O., Linders, T. and Debernard, J.B. (2008) Can polar lows lead to a warming of the ocean surface? *Tellus A: Dynamic Meteorology and Oceanography*, 60, 141–153.

Terpstra, A., Renfrew, I.A. and Sergeev, D.E. (2021) Characteristics of cold air outbreaks and associated polar mesoscale cyclogenesis over the North Atlantic region. *Journal of Climate*, 34, 4567–4584. https://doi.org/10.1175/JCLI-D-20-0595.1.

Våge, K., Moore, G.W.K., Jónsson, S. and Valdimarsson, H. (2015) Water mass transformation in the Iceland Sea. *Deep Sea Research Part I: Oceanographic Research Papers*, 101, 98–109.

Våge, K., Papritz, L., Håvik, L., Spall, M.A. and Moore, G.W.K. (2018) Ocean convection linked to the recent ice edge retreat along East Greenland. *Nature Communications*, 9, 1287.

Våge, K., Pickart, R.S., Moore, G.W.K. and Ribergaard, M.H. (2008) Winter mixed layer development in the central Irminger Sea: the effect of strong, intermittent wind events. *Journal of Physical Oceanography*, 38, 541–565.

Våge, K., Pickart, R.S., Spall, M.A., Valdimarsson, H., Jónsson, S., Torres, D.J., Østerhus, S. and Eldevik, T. (2011) Significant role of the north Icelandic jet in the formation of Denmark Strait overflow water. *Nature Geoscience*, 4, 723–727.

Våge, K., Semper, S., Valdimarsson, H., Jónsson, S., Pickart, R.S. and Moore, G.W.K. (2022) Water mass transformation in the Iceland Sea: contrasting two winters separated by four decades. *Deep Sea Research.* 101, 98–109. https://doi.org/10.1016/j.dsr.2022.103824.

Våge, K., Spengler, T., Davies, H.C. and Pickart, R.S. (2009) Multi-event analysis of the westerly Greenland tip jet based upon 45 winters in ERA-40. *Quarterly Journal of the Royal Meteorological Society*, 135, 1999–2011.

Wong, A.P., et al. (2020) Argo data 1999–2019: two million temperature-salinity profiles and subsurface velocity observations from a global array of profiling floats. *Frontiers in Marine Science*, 7, 700. https://doi.org/10.3389/fmars.2020.00700.